NECAB2 orchestrates an endosomal pathway of mitochondrial quality control at striatal synapses

Partha Narayan Dey[1]*, Diones Bueno[1]*, Teresa Schacht[1]*, Christina Wolf[1], Verena Wüllner[1], Elena Morpurgo[1], Liliana Rojas-Charry[1,9], Lena Sessinghaus[2], Petra Leukel[2], Clemens Sommer[2], Konstantin Radyushkin[3], Michael K.E. Schäfer[4], Luise Florin[5], Stefan Tenzer[6], Jan Baumgart[7], Paul Stamm[8], Andreas Daiber[8], Guilherme Horta[9], Leonardo Nardi[9], Verica Vasic[9], Michael J. Schmeisser[9], Andrea Hellwig[10], Angela Oskamp[11], Andreas Bauer[11], Ruchika Anand[12], Andreas S. Reichert[12], Sandra Ritz[13], Marion Silies[14], Katrin B. M. Frauenknecht[2,15], and Axel Methner[1]#

University Medical Center of the Johannes Gutenberg-University Mainz: [1]Institute for Molecular Medicine, [2]Institute of Neuropathology, [3]Mouse Behavior Unit, [4]Department of Anesthesiology, [5]Institute for Virology, [6]Institute of Immunology, [7]Translational Animal Research Center (TARC), [8]Center for Cardiology, [9]Institute for Microscopic Anatomy and Neurobiology. [10]Department of Neurobiology, Interdisciplinary Center for Neurosciences (IZN), Heidelberg University, Germany. [11]Institute of Neuroscience and Medicine (INM-2), Forschungszentrum Jülich GmbH, Germany. [12]Institute of Biochemistry and Molecular Biology I, Medical faculty, Heinrich Heine University Düsseldorf, Düsseldorf, Germany. [13]Institute of Molecular Biology gGmbH (IMB), Mainz, Germany. [14]Institute of Developmental Biology and Neurobiology, Johannes Gutenberg-University Mainz, [15]Institute of Neuropathology, University and University Hospital Zurich, Switzerland

#Address for correspondence: Axel Methner MD, University Medical Center of the Johannes Gutenberg-University Mainz, Institute for Molecular Medicine, Langenbeckstr. 1, D-55131 Mainz, Germany, Tel.: +49-6131-17-2695, Fax: +49-6131-17-5967, Email: axel.methner@gmail.com

Summary

Synaptic signaling depends on ATP generated by mitochondria. Due to extensive connectivity, the striatum is especially vulnerable to mitochondrial dysfunction and thus requires efficient mitochondrial quality control. We found that the neuronal calcium-binding protein NECAB2 ensures synaptic function in the striatum by increasing mitochondrial efficiency. NECAB2 associates with early endosomes and mitochondria at striatal synapses. Loss of NECAB2 dysregulates proteins of the endosomal ESCRT machinery and oxidative phosphorylation. Mitochondria from NECAB2-deficient mice are more abundant but less efficient. These mitochondria exhibit increased respiration and superoxide production but produce less ATP. This accumulation of faulty mitochondria is caused by a defective assembly of mitochondria with early endosomes in response to oxidative stress. Impairment of this mechanism causes loss of striatal synapses and behavioral dysfunctions such as reduced motivation and altered sensory gating. NECAB2 therefore orchestrates an endosomal pathway of mitochondrial quality control important for striatal function.

Introduction

The striatum is an important brain structure involved in motor and action planning, decision-making, motivation and reward (Cox & Witten, 2019). Afferent and efferent projections from the striatum project to other brain regions such as the cortex, thalamus and the substantia nigra (Cox & Witten, 2019). The integrity of this system critically depends on mitochondrial energy production because either mitochondrial disease, depletion of mitochondria, or mitochondrial toxins specifically induce striatal degeneration. A point mutation in mitochondrial DNA results in a specific striatal degeneration called Leber's disease (Novotny *et al*, 1986), depletion of mitochondrial DNA (Pickrell *et al*, 2011) also causes striatal degeneration, as does ingestion of the mitochondrial toxin 3-nitropropionic acid (reviewed in (Brouillet *et al*, 2005)). Furthermore, Huntington's disease (HD), a hereditary disorder caused by an expanded poly-glutamine in the ubiquitously expressed protein huntingtin, causes striatal degeneration and is associated with mitochondrial dysfunction (reviewed in (Bates *et al*, 2015)).

It is therefore evident that the striatum depends on the optimal functioning of mitochondria – even more so than other parts of the brain. The reasons are unknown but might be attributed to the high energy demands of the glutamatergic input from both the cortex and thalamus as well as the dopaminergic input from the midbrain. Synaptic signaling consumes a substantial amount of the total ATP generated in the brain. Specifically, glutamatergic synapses have very high energy demands required to reverse the ion movements that generate postsynaptic responses (Harris *et al*, 2012).

Cells adapt the amount and quality of mitochondria to their metabolic demand by a process called mitochondria quality control which either removes unfit mitochondria via selective mitophagy or oxidized pieces of mitochondria via mitochondria-derived vesicles. Of note, most of these processes involve PTEN-induced putative kinase protein 1 (PINK1) and the E3 ubiquitin ligase Parkin (Clark *et al*, 2006; Park *et al*, 2006). In healthy mitochondria, PINK1 is imported and rapidly degraded, but in unfit mitochondria with a reduced mitochondrial membrane potential ($\Delta\psi_m$), PINK1 import is stalled, leaving enough PINK1 at the outer mitochondrial membrane to phosphorylate Parkin. Parkin then ubiquitinates itself and proteins of the outer mitochondrial membrane (Sarraf *et al*, 2013) resulting in mitophagy (reviewed by (Narendra *et al*, 2012)). Importantly, basal mitophagy *in vivo* occurs even in the absence of the PINK1/Parkin pathway in all tissues with high metabolic demand including the brain (McWilliams *et al*, 2018). Recently, two alternative mechanisms of mitochondrial quality control involving Ras-related protein Rab-5 (RAB5)-positive early endosomes were described. These can be triggered either by dissipation of $\Delta\psi_m$ involving Parkin and the endosomal sorting complexes required for transport (ESCRT) machinery (Hammerling *et al*,

2017), or by oxidative stress elicited by hydrogen peroxide (H_2O_2) (Hsu *et al*, 2018). While it is conceivable that mitochondrial quality control is important for striatal function, the relevance of these novel pathways of mitochondrial quality control for striatal function is unclear.

The striatum is the major site of expression of the neuronal Ca^{2+}-binding protein 2 (NECAB2), a largely uncharacterized protein containing two EF-hand Ca^{2+}-binding domains and a so-called antibiotic biosynthesis monooxygenase (ABM) domain connected by two coiled-coil domains. NECAB2 has two 39 kDa and 43 kDa splice isoforms that differ in 37 amino acids at the N-terminal part of the molecule (Canela *et al,* 2007). In the striatum, NECAB2 co-localizes and interacts with the G-protein coupled receptors (GPCRs) adenosine A_{2A} receptor ($A_{2A}R$) (Canela *et al,* 2007) and the metabotropic glutamate receptor 5 ($mGluR_5$) (Canela *et al,* 2009). Functionally, the presence of NECAB2 increases receptor surface localization and basal signal transduction via extracellular signal regulated kinases (ERK) 1 and 2 (Canela *et al*, 2009; 2007). The interaction of NECAB2 with either receptor decreases in the presence of high Ca^{2+} levels (Canela *et al*, 2009; 2007). Activation of both receptors increases NMDA receptor-mediated Ca^{2+} entry from the extracellular space in striatal neurons (Higley & Sabatini, 2010; Pisani *et al,* 2001). In addition, $mGluR_5$ activation also causes Ca^{2+} release from the endoplasmic reticulum (ER). Taken together, these findings suggest that in quiescent neurons with low Ca^{2+} levels, NECAB2 boosts basal $A_{2A}R$ and $mGluR_5$ signal transduction by favoring surface localization of GPCRs, whereas upon increases in Ca^{2+} levels – either through activation of GPCRs or synaptic stimulation – NECAB2 dissociates from the GPCRs, together forming a negative feedback loop.

Ca^{2+} binding is mediated by the EF hands and protein-protein interaction by one of the coiled-coil domains (Canela *et al,* 2007). The role of the ABM domain in this process is however less obvious. Besides the highly homologous NECAB1 and NECAB3 proteins, ABM domains are only found in a group of atypical heme monooxygenases from bacterial species (reviewed by (Lyles & Eichenbaum, 2018)) and unicellular green algae (Lojek *et al*, 2017) but not in any other mammalian protein. The substrate of this enzymatic activity and the role of this hypothetical mechanism for striatal function are unclear.

We here studied the role of NECAB2 in striatal brain function and found that global knockout of NECAB2 in the mouse causes a profound dysfunction of mitochondrial quality control mediated by the endosomal ESCRT system. Without NECAB2, hydrogen peroxide loses its ability to trigger the association of RAB5-positive endosomes with mitochondria. In line with the dysfunctional quality control, mitochondria from *Necab2* knockout mice are more abundant but less efficient. They are characterized by increased respiration and superoxide production but generate less ATP. Absence of this pathway causes loss of striatal synapses and behavioral phenotypes related to striatal dysfunction such as reduced motivation and

altered sensory gating. NECAB2 therefore ensures mitochondrial efficiency in response to high energetic demand in active neurons by a novel endosomal quality control pathway.

Results

NECAB2 is expressed in a punctate synaptic and neuronal pattern in the striatum of mice and men

To elucidate the role of NECAB2 in brain function, we first investigated the expression pattern of NECAB2 in the mouse and human brain using immunohistochemistry. This demonstrated that NECAB2 is strongly expressed in the mouse caudate putamen (the striatum), the hippocampal CA2 region, the indusium griseum, habenulae, fasciculus retroflexus, and the substantia nigra (Figure 1A). In the human striatum, NECAB2 is prominently expressed in neurons and the neuropil of the putamen and slightly less in the caudate nucleus (Figure 1B). These two structures constitute the human equivalent of the rodent striatum. In the globus pallidus externus and internus only the neuropil but not the somata of neurons are stained (Figure 1B). The majority of synapses of pallidal neurons represent striatopallidal terminals. Within the striatum, the vast majority of neurons are GABAergic inhibitory medium spiny neurons (MSNs), which are characterized by large and extensive dendritic trees and a high abundance of spines. There are at least two subtypes of MSNs: direct pathway MSNs excite their ultimate basal ganglia output structure and express dopamine D1 receptors and adenosine A1 receptors, while indirect pathway MSNs inhibit their output structure and express dopamine D2 receptors and NECAB2-interacting $A_{2A}R$ receptors. Using mice that express tagged dopamine D1 and D2 receptors (Thibault *et al*, 2013), we found NECAB2 expressed in MSNs of both the direct and indirect pathway (Figure 1C). In mice and men, NECAB2 immunoreactivity is mainly present in intracellular punctate structures located in the somatodendritic and synaptic compartments of medium spiny neurons. We therefore studied the cellular localization of NECAB2 in relation to synaptic marker proteins that label the presynaptic glutamatergic terminals of corticostriatal (VGLUT1) and thalamostriatal (VGLUT2) synapses. This demonstrated that NECAB2 punctae are adjacent to and partially overlapping with VGLUT1 or VGLUT2 signals (Figure 1D), implicating localization of NECAB2 on the postsynaptic side. Together these results suggest a role for NECAB2 in organelle function and synaptic signaling in the striatum.

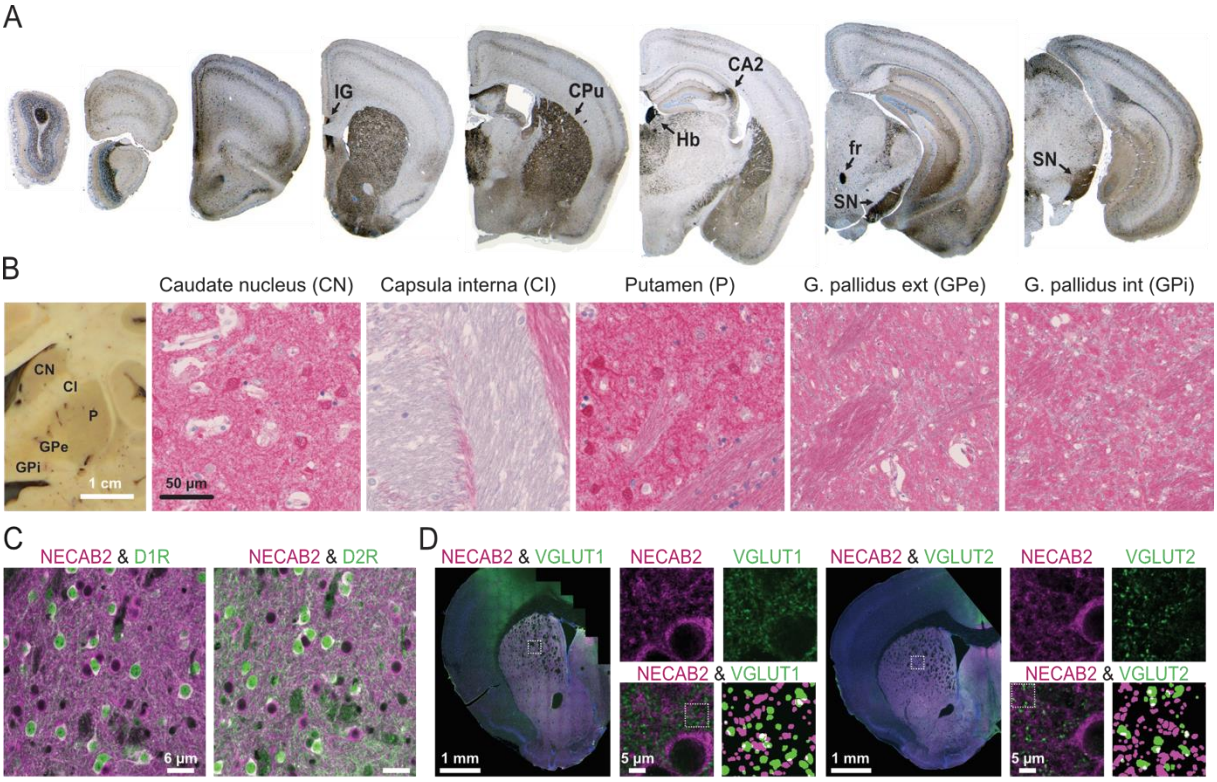

Figure 1 NECAB2 is expressed in a punctate synaptic and neuronal pattern in the striatum of mice and men. (A,B) Immunohistochemical staining demonstrates prominent expression of NECAB2 in (A) the mouse striatum (caudate putamen, CPu), the CA2 region of the hippocampus, indusium griseum (IG), habenulae (Hb), fasciculus retroflexus (fr), and substantia nigra (SN). (B) In the human striatum, which is composed of the caudate nucleus and the putamen, NECAB2 is expressed intracytoplasmically in neurons and in a punctate synaptic pattern in the neuropil. (C) NECAB2 is expressed in medium spiny neurons of the direct (D1R+) and indirect (D2R+) pathway assessed by immunohistochemistry in D1R-tdtomato und D2R-GFP-overexpressing mice. (D) In the mouse striatum, NECAB2 has a punctate staining pattern located in the somatodendritic and synaptic compartments of medium spiny neurons. Partial overlap with both VGLUT1 and VGLUT2 indicates its postsynaptic localization at both corticostriatal and thalamostriatal contacts.

NECAB2 deficiency dysregulates mitochondrial and endosomal proteins

To investigate if NECAB2 deficiency affects striatal functions, we studied mice with a global knockout (KO) of *Necab2*. An antiserum specific to NECAB2 demonstrated a complete loss of protein expression in the striatum by immunochemistry and immunoblotting (Figure 2A). Using autoradiography, we investigated changes in the abundance of the GPCRs interacting with NECAB2 ($A_{2A}R$ and $mGluR_5$), of receptors known to heterodimerize with these GPCRs (Ferré *et al*, 2002) that define MSN subsets (D1R and D2R), and of the dopamine transporter (DAT) as a general striatal marker and found no differences in binding density between wildtype and *Necab2* KO mice (Figure 2B). Also baseline ERK1 and 2 phosphorylation was similar in wildtype (WT) and KO mice (Figure 2C) despite the positive effect of overexpressed NECAB2 on $A_{2A}R$ (Canela *et al*, 2007) and $mGluR_5$-mediated ERK1/2 phosphorylation in human embryonic kidney cells (Canela *et al*, 2009). *Necab2* deficiency

therefore does not alter the function or abundance of striatal GPCRs – suggesting additional, novel roles for NECAB2.

To identify such additional NECAB2 functions, we compared the relative protein abundance in the striatum of WT and *Necab2* KO mice using label-free proteomics. This demonstrated a significant amount of dysregulated proteins with the most prominently altered pathways being related to the endosomal ESCRT machinery and cellular respiration (Figure 2D). These data suggest that loss of NECAB2 function affects pathways related to the correct functioning of endosomes and mitochondria.

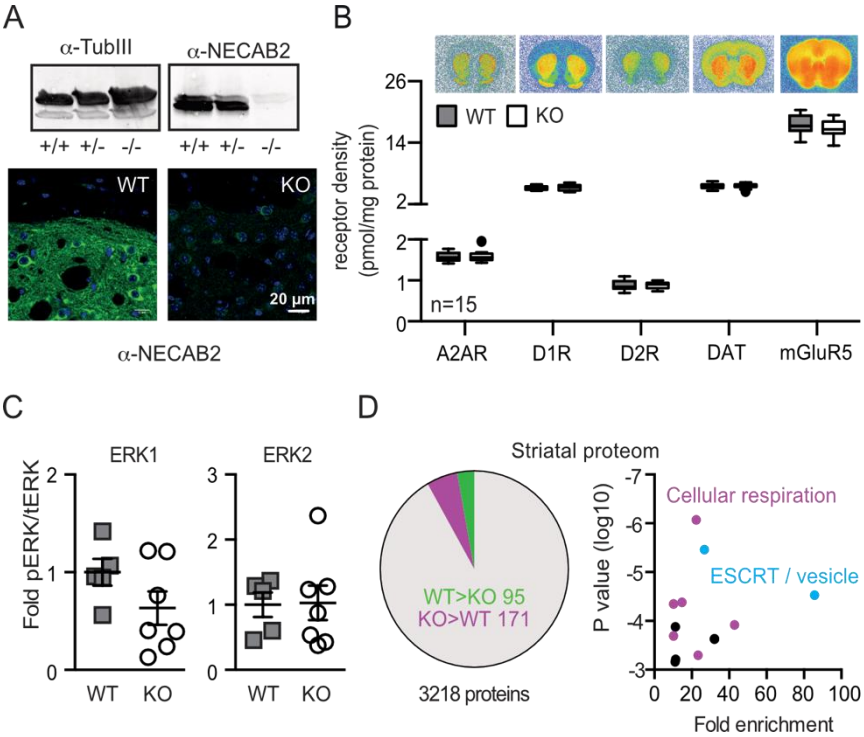

Figure 2 NECAB2 deficiency dysregulates mitochondrial and endosomal proteins. (A) Validation of NECAB2 deficiency and antibody specificity in -/- mice shown by immunoblotting and immunohistochemical staining of striatal tissue. (B) No differences in receptor density of striatal receptors $A_{2A}R$, $mGluR_5$, D1R, D2R and the dopamine transporter (DAT) in wildtype (WT) and *Necab2* knockout (KO) mice measured by receptor autoradiography. Data represent Tukey plots obtained from 15 WT and KO mice. (C) Similar ERK phosphorylation between WT and KO striatal tissue. Each data point represents the ratio of phosphorylated and total ERK from one mouse quantitated by immunoblotting. (D) Number of all proteins and regulated proteins in the striatal proteome of indicated samples obtained from n=3 (WT) and n=5 (KO) mice identified by label-free quantitative proteomics. Gene ontology classification of proteins dysregulated in *Necab2* KO demonstrates alterations of proteins involved in ESCRT and cellular respiration in whole striatal tissue.

NECAB2 co-localizes with mitochondria and early endosomes

To clarify the identity of the intracellular NECAB2-immunopositive punctate structures observed in Figure 1, we next co-expressed tagged NECAB2 with fluorescent proteins directed to specific intracellular organelles in hippocampal HT22 cells. This revealed co-localization with mitochondria and endosomes (CD63) in line with functional alterations of

these organelles observed in the proteome analysis, but no co-localization with autophagosomes (LC3B) or the ER (Supplemental Figure S1). We confirmed this localization in primary striatal neurons using RAB5 as an early endosomal and the 75 kDa glucose-regulated protein (GRP75) as a mitochondrial marker (Figure 3A). Furthermore, NECAB2 is present in early endosomal fractions (Figure 3B) and in fractions containing synaptic but not non-synaptic mitochondria (Figure 3C). Proteinase K digestion of the mitochondrial fraction effaced immunoreactivity against NECAB2 and the voltage-dependent anion channel (VDAC) at the outer mitochondrial membrane but not against the matrix protein cytochrome *c* oxidase (Figure 3D) indicating that mitochondrial NECAB2 associates with the outer mitochondrial membrane. To corroborate the unexpected partial mitochondrial localization of NECAB2, we stained striatal tissue sections with antibodies against NECAB2 and the mitochondrial marker protein cytochrome *c.* This revealed the presence of cytochrome *c*-positive structures within NECAB2-stained areas (Figure 3E). Together with the proteome analysis, these results suggest a role for NECAB2 at the interface of mitochondrial and endosomal function at striatal synapses.

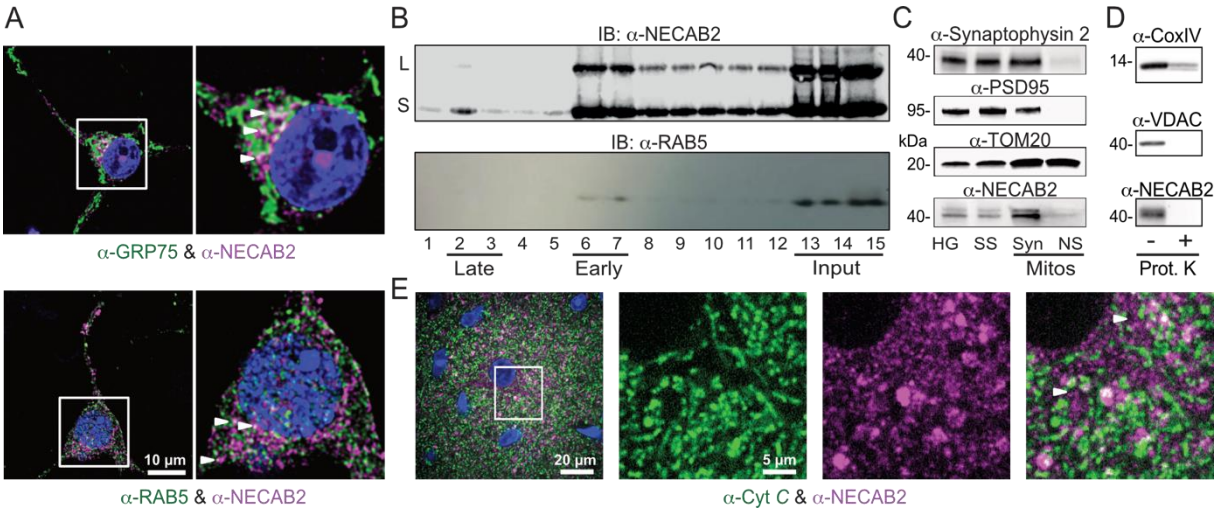

Figure 3 NECAB2 co-localizes with mitochondria and early endosomes. (A) Punctate pattern of NECAB2 staining in primary striatal cultures and partial co-localization with the mitochondrial marker GRP75 and the endosome marker RAB5. (B) Presence of NECAB2 in immunoblotted endosomal fractions. L and S represent the long and short splice isoforms of NECAB2. RAB5 served as control. (C) Presence of NECAB2 in fractions containing synaptic but not non-synaptic mitochondria. PSD95 and synaptophysin-2 served as synaptic markers, TOM20 as mitochondrial marker protein. (D) In mitochondrial fractions, NECAB2 can be digested with proteinase K suggesting its presence at the outer mitochondrial membrane. VDAC as outer mitochondrial membrane protein and cytochrome oxidase IV (CoxIV) as mitochondrial matrix protein served as controls. (E) Immunohistochemical co-staining of NECAB2 and the mitochondrial protein Cytochrome *c* (Cyt C) in striatal tissue sections demonstrating that NECAB2-positive punctae contain mitochondrial material.

Mitochondrial NECAB2 exists predominantly as a dimer

NECAB2 contains a so-called ABM domain with a potential enzymatic activity as a heme oxygenase essentially found only in prokaryotes (Lyles & Eichenbaum, 2018). As these

prokaryotic ABM proteins exert their enzymatic function as homodimers (Lyles & Eichenbaum, 2018), we posited that NECAB2 can also exist in a dimeric state and in fact found dimeric and possibly even multimeric NECAB2 in striatal tissue immunoblotted on non-reducing gels (Figure 4A). This dimeric form is significantly more prevalent in mitochondrial fractions obtained from mouse striata, even in reducing gels (Figure 4B). Modeling the structure of NECAB2 based on the bacterial ABM domain structure revealed that NECAB2 has four domains, the EF hand domain, two coiled-coil regions, and the ABM domain (Figure 4C). We generated stable neuronal cell lines expressing wildtype NECAB2, NECAB2 expressing mutated EF hands (mEF, E84A/E118A), or NECAB2 lacking the specific distinguishable domains. Immunoblotting of protein lysates from these cell lines demonstrated that NECAB2 proteins lacking the CC1 and the ABM domain do not dimerize and that expression in the ΔCC1 mutant is consistently weaker than in other mutants (Figure 4D).

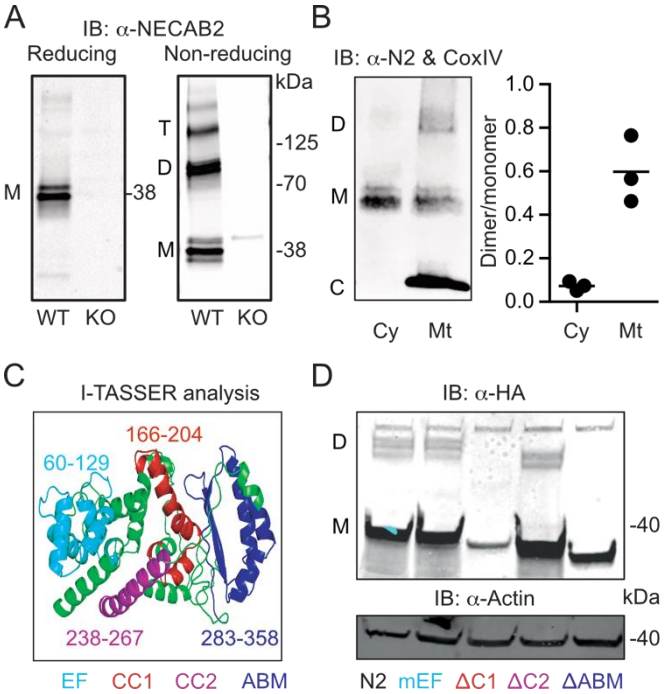

Figure 4 NECAB2 dimerizes in mitochondria via its ABM domain. (A and B) Mitochondrial NECAB2 forms dimers on (A) non-denaturing gels, which (B) are enriched in mitochondrial fractions. D, dimer; M, monomer; C, CoxIV as a mitochondrial marker protein. (C) Model of NECAB2 and its distinct domains with boundaries. (D) Immunoblotting stable cell lines expressing HA-tagged full-length NECAB2 or NECAB2 with mutated EF hand (E84A/E118A, mEF) or lacking CC1 (ΔC1), CC2 (ΔC2) or the AMB domain (ΔABM) reveals loss of dimerization in the ΔCC1 and ΔABM mutants.

We conclude from these experiments that NECAB2 dimerizes via its ABM domain similarly to prokaryotic ABM-containing proteins. The CC1 domain that interacts with mGluR5 (Canela *et al*, 2007) also appears to be necessary for dimerization. However, the less efficient expression of this mutant in the immunoblots could indicate that loss of this domain disrupts protein folding, thereby rendering the true interaction domains inaccessible. The fact that the

dimer is more prevalent in mitochondrial fractions implies that the potential enzymatic activity of NECAB2 could be involved in the function of NECAB2 at the interface between mitochondria and endosomes.

Necab2 knockout uncouples mitochondrial respiration and ATP generation

Since the proteome analysis suggested changes in mitochondrial function, we next assessed the morphology of mitochondria using transmission electron microscopy. Because NECAB2 is localized at striatal synapses (Figure 1D) and in fractions enriched in synaptic mitochondria (Figure 3C), we first used synaptosomes. NECAB2 is indeed abundant in the striatal synaptosomes used for the analysis (Figure 5A). *Necab2 KO* mitochondria were significantly smaller and had a higher electron density than those of wildtype samples (Figure 5B). Higher electron density is frequently associated with an increased activity of the respiratory chain (Hackenbrock, 1966). The same mitochondrial morphology and electron density was also evident in tissue sections of the striatum of *Necab2 KO* mice (Figure 5C). Striatal sections of the KO also had an increased number of mitochondria (Figure 5D).

We then investigated the efficiency of oxidative phosphorylation, the oxygen-dependent production of ATP driven by the electrochemical gradient across the inner mitochondrial membrane, in *Necab2* KO mice. High-resolution respirometry of striatal tissue demonstrated an increased respiration in the absence of NECAB2 in line with the higher electron density of KO mitochondria observed. Normalizing respiration to the maximum electron transfer capacity (ETS) revealed that *Necab2* KO mitochondria spend a higher proportion of their maximum capacity for routine respiration thus reducing their spare capacity (Figure 5E). Primary striatal cultures from the *Necab2* KO also showed a more negative mitochondrial membrane potential ($\Delta\psi m$) revealed by the mitochondrial membrane dye TMRM (Figure 5F). Treatment with the mitochondrial uncoupler trifluoromethoxy carbonyl cyanide phenylhydrazone (FCCP) collapsed $\Delta\psi m$, validating the measurements. Therefore, both respiration and membrane potential, demonstrated an increased activity of *Necab2* KO mitochondria.

However, KO mitochondria in striatal cultures generated less ATP, quantified with the ratiometric ATP sensors BTeam (Yoshida *et al*, 2016) targeted to the cytosol or the mitochondrial matrix (Figure 5G). *Necab2* KO mitochondria produced more superoxide as shown in striatal primary culture by staining with the dye MitoSOX (Figure 5H) or *in situ* as assessed by quantifying oxidized 2-hydroxyethidium by high-performance liquid chromatography in striatal tissue treated with the complex III inhibitor myxothiazol (Kröller-Schön *et al*, 2014) (Figure 5I). We also detected increased amounts of oxidized DNA in striatal tissue using an antibody against 8-hydroxy-2'-deoxyguanosine (Figure 5J) and reduced levels of the major antioxidant glutathione in the striata of adult mice (Figure 5K) in

line with a more oxidative environment. Together, these data demonstrate that striatal mitochondria from *Necab2* KO mice are more abundant but less efficient. They exhibit an increased respiration and superoxide production but generate less ATP.

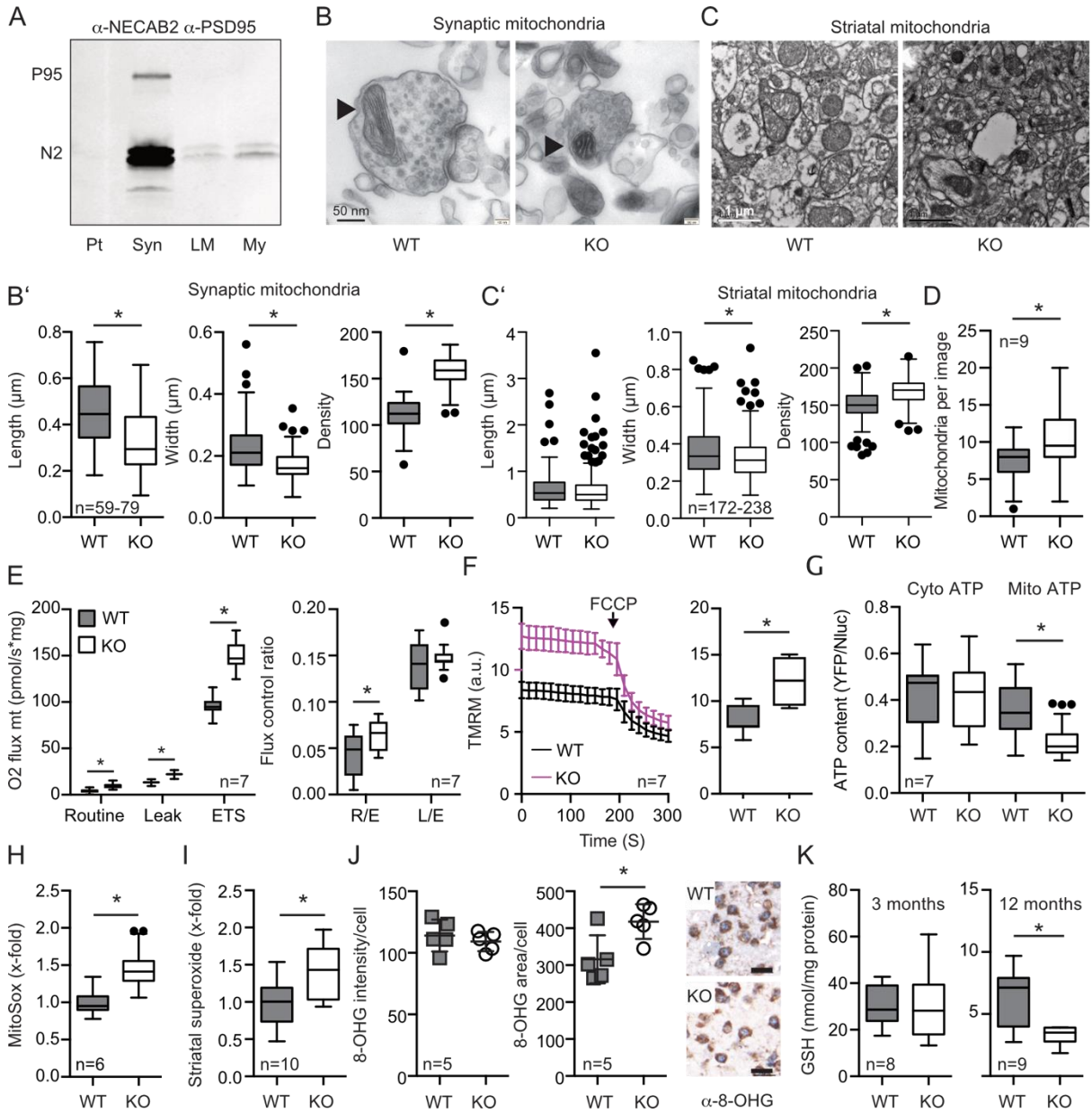

Figure 5 *Necab2* knockout uncouples mitochondrial respiration and ATP generation. (A) Immunoblot showing that NECAB2 is enriched in synaptosomes (Syn) but less in pellet (Pt), light membrane (LM) and myelin (My) containing fractions. PSD95 serves as a synaptic marker. (B,C) Transmission electron microscopy demonstrates morphological alterations of mitochondria in (B) striatal synaptosomes, n=59-79 synapses from 10 mice and in (C) striatal tissue, n=172-238 synapses from 5 mice. KO mitochondria were significantly smaller and showed a higher electron density. (D) Increased number of mitochondria in striatal tissue of the KO, quantified per visual field, n=48 from 9 mice. (E) Increased respiration of KO mitochondria shown by high-resolution respirometry of striatal tissue. Leak respiration was measured after addition of oligomycin to inhibit the ATP synthase and the electron transfer system (ETS) capacity after titration of FCCP. Flux control ratios are obtained by dividing routine (R) and leak (L) respiration with the ETS (E) values, n=7 mice. (F) *Necab2* KO mitochondria show an increased mitochondrial membrane potential (Δψm) in primary striatal cultures stained with TMRM. Δψm collapses after addition of the uncoupler FCCP, n=7 independent cultures. (G) Reduced mitochondrial ATP

content despite increased respiration of primary striatal cultures shown with the ratiometric ATP reporter BTeam. n=7 independent cultures. (H) Increased mitochondrial superoxide production in primary striatal cultures shown by staining with MitoSOX, n=6 independent cultures, and (I) in striatal KO tissue treated with the complex III inhibitor myxothiazol. Superoxide formation was quantitated by the dihydroethidium oxidation product 2-hydroxyethidium detected by its fluorescence at 480/580 nm (Ex/Em) and normalized to wet weight, n=10 mice (J) Increased immunohistochemical staining of the reactive oxygen species marker 8-hydroxyguanine (8-OHG) in KO striata. Scale bar represents 20 µm. Each data point contains the mean of n=10 cells analyzed from 5 mice, *<0.05 Mann Whitney test. (K) Reduced striatal total glutathione determined enzymatically in adult but not juvenile KO mice, n=6-9 mice. Data are presented as Tukey plots, *<0.05 Mann Whitney test.

NECAB2 deficiency abrogates endosomal mitochondrial quality control elicited by oxidative stress

The preponderance of less efficient mitochondria together with alterations in proteins of the ESCRT machinery in the absence of NECAB2 (Figure 2D) and the engulfment of mitochondrial structures by NECAB2-stained vesicular structures (Figure 3E), suggest that mitochondrial proteins are less efficiently recycled or repaired by endosomes in the *Necab2 KO*. In line with this hypothesis, we observed an increased abundance of respiratory chain proteins measured by label-free proteomics in whole striatal samples from *Necab2* KO mice in line with the increased number of mitochondria but a decreased abundance in striatal endosomal fractions (Figure 6A). Two recently described and probably distinct pathways of mitochondrial quality control involving RAB5-positive early endosomes can be triggered either by dissipation of the mitochondrial membrane potential, involving PINK1/Parkin (Hammerling *et al*, 2017) or by oxidative stress (Hsu *et al*, 2018). To test and distinguish these two pathways, we treated mature primary striatal cultures from WT and KO littermates with FCCP or H_2O_2 and quantified endosomes alone, as well as endosomes associated with mitochondria (see exemplary striatal neuron with labeled endosomes and mitochondria in Figure 6B).

When comparing just RAB5-positive endosomes, this demonstrated a similar increase in WT and KO neurons upon treatment with FCCP and no changes with H_2O_2 (Figure 6C). The abundance of structures positive for both RAB5 and TOM20 (translocase of outer membrane 20, a mitochondrial marker protein) was however different between WT and *Necab2* KO. When treated with H_2O_2, WT showed a not significant increase in double-positive structures, whereas their number significantly declined in the KO (Figure 6D). In contrast, when treated with FCCP, WT mice tended to show less double-positive structure, which however significantly increased in KO (Figure 6D). Together, our data argue that the H_2O_2-mediated pathway is defective in *Necab2* KO animals and causes the less efficient recycling or repair of mitochondria in the *Necab2* KO. The upregulation of double-positive structures in KO upon exposure to FCCP could be interpreted as a compensatory upregulation of the PINK1/Parkin endosomal pathway.

We therefore further tested the requirement of NECAB2 for mitochondrial quality control triggered by oxidative signaling. We studied the recruitment of RAB5-positive endosomes to TOM20-positive structures by measuring the shortest distance between the surfaces of these structures. Here, negative values denote the presence of TOM20 signal within RAB5-positive structures. WT animals showed the previously described (Hsu *et al*, 2018) recruitment of RAB5-positive endosomes to mitochondria upon H_2O_2 challenge while this was absent in *Necab2* KO striatal neurons (Figure 6E). Finally, NECAB2 co-localization with endosomes and mitochondria decreased upon H_2O_2 treatment (Figure 6F) suggesting that NECAB2 probably moves to the plasma membrane to rendezvous with GPCRs (Canela *et al*, 2009; 2007). We conclude that NECAB2 is necessary for the endosomal pathway of mitochondrial quality control triggered by oxidative signaling.

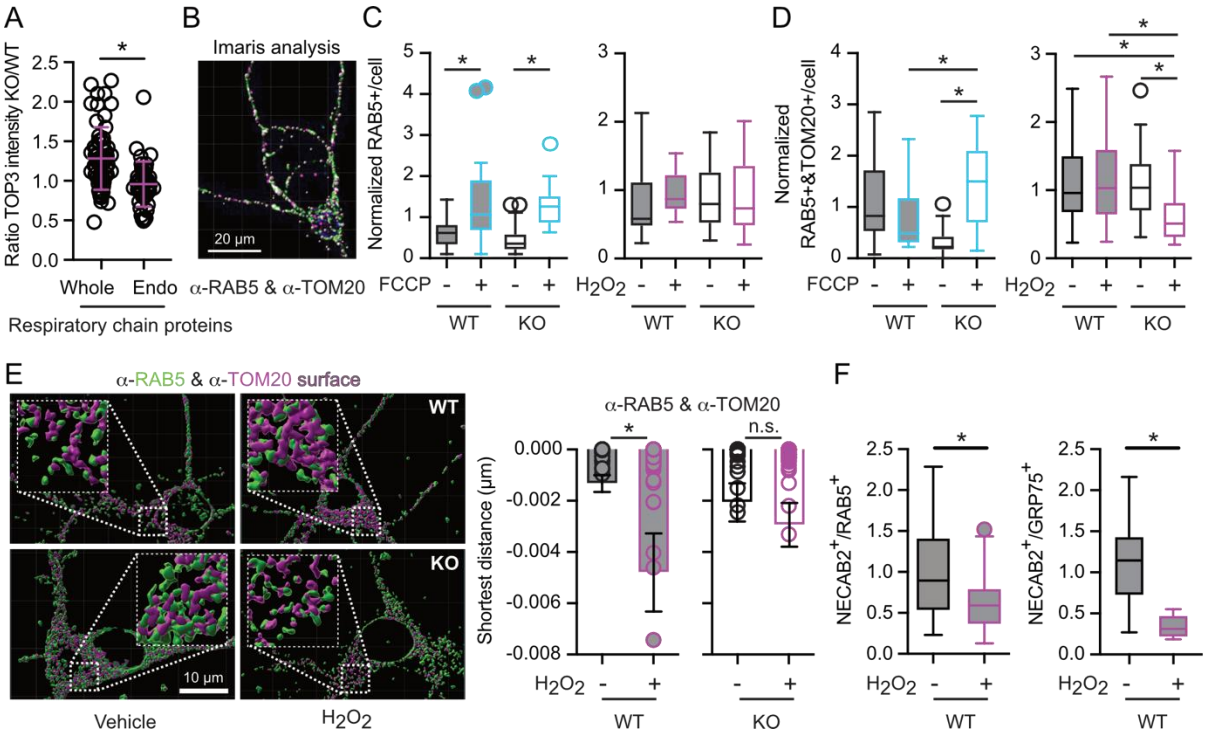

Figure 6. NECAB2 deficiency abrogates endosomal mitochondrial quality control elicited by hydrogen peroxide. (A) The ratio of respiratory chain proteins quantified by label-free proteomics in KO and WT demonstrates increased abundance of mitochondrial proteins in whole striatal KO tissue with reduced abundance in striatal endosomal fractions. (B) Exemplary neuron from primary striatal cultures at DIV 14 stained against RAB5 and TOM20. (C, D) Primary striatal cultures at DIV 12-14 from WT and KO littermates were treated with 10 µM FCCP or 100 µM H_2O_2 for 2 h and (C) the number of RAB5 respectively (D) RAB5 and TOM20-positive structures quantified with Imaris. This demonstrated opposing changes in WT and KO neurons. (E) Exemplary neurons from primary striatal cultures at DIV 14 stained against. Stacked images were used to generate surfaces from the fluorescent signal using the Imaris software. The generated surfaces were used to calculate the distance and the number and distance of contact points between TOM20 and RAB5-positive punctae. 100 µM H_2O_2 induces an approximation between the RAB5 and TOM20 punctae only in the WT. Data are presented as individual data points with mean ± SEM or as Tukey plots. (A) n=3-4 animals, each circle represents the KO/WT ratio of one protein, *<0.0001 Mann Whitney test. (C/D) n=15-37 neurons from 3 mice per genotype, *<0.05 one-

way ANOVA. (E) n=48-64 neurons from 3 mice per genotype is indicated, only data points < 0 are shown, *<0.05 Mann Whitney test. (F) n=9-47 neurons from 3 mice per genotype. *<0.05 Mann Whitney test.

NECAB2 deficiency causes striatal dysfunction by loss of striatal synapses

Based on the importance of mitochondria for synaptic function, we next asked whether disruption of NECAB2-mediated mitochondrial quality control results in morphological and behavioral alterations associated with synaptic dysfunction. We analyzed differences in dendritic arborization and spine density of MSNs using the Golgi-Cox technique. This revealed a similar length, but decreased quantity of dendrites in KO animals (Figure 7A) as well as an increased spine density (Figure 7B). Spine density might serve to compensate for the fewer dendrites. To confirm this finding, we also quantified spines from mice that were *in-utero* electroporated with a vector expressing GFP (Figure 7C). This again demonstrated an increased spine density in *Necab2* KO mouse. In addition, *Necab2* KO mice had a reduced number of striatal synapses shown by immunohistochemistry using the presynaptic marker protein vesicle-associated membrane protein 2 (VAMP2), (Figure 7D). This reduced number of striatal synapses was further confirmed by TEM analysis (Figure 7E).

To study behavioral consequences of NECAB2 dysfunction, we then focused on behavioral functions of the striatum, the major site of NECAB2 expression. In this location, GABAergic striatal MSNs are critical for motor control and play an important role in motivation and reward. We used 15 adult male WT and KO mice and analyzed their behavior using well-established tests. First of all, basic locomotion tested by the open field test or the elevated plus maze test were not impaired (Supplemental Figure S2). However, in line with striatal and basal ganglia dysfunction, we found reduced motivation in the progressive ratio schedule test, increased catalepsy, and reduced sensory gating as analyzed by pre-pulse inhibition of the startle response in KO mice (Figure 7F).

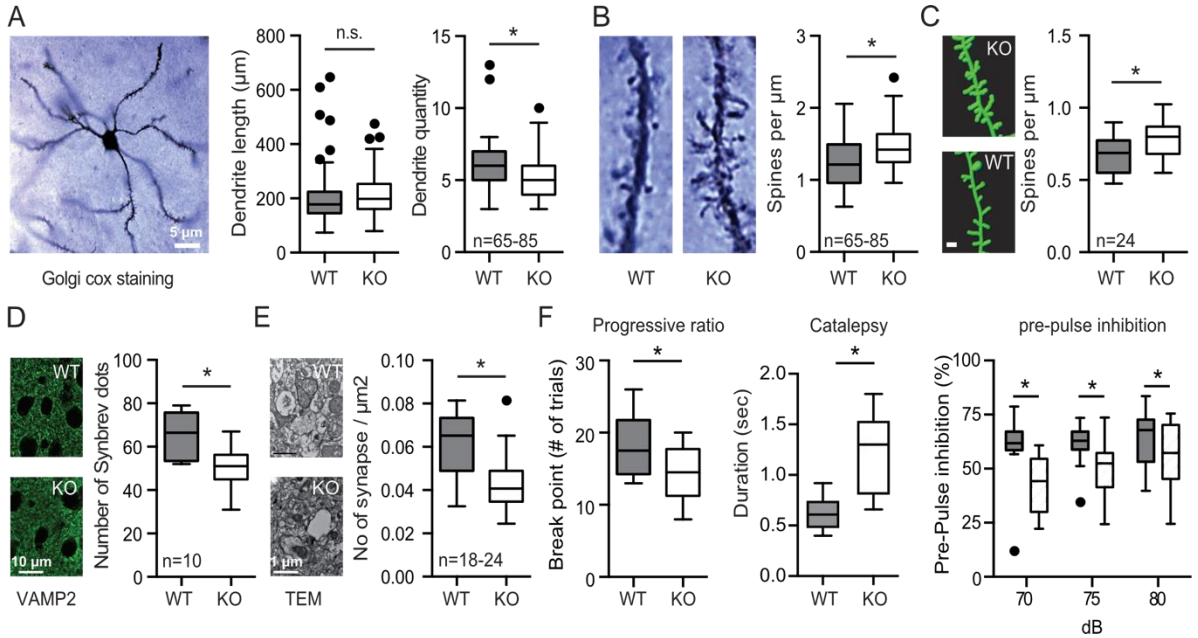

Figure 7 NECAB2 deficiency causes loss of striatal synapses and behavioral deficits associated with striatal dysfunction. (A,B) Golgi cox staining demonstrates (A) a decreased dendrite quantity but (B) more spines per µm. (C) Similar increase in striatal spine density in in-utero electroporated mice expressing GFP. Scale bar 1 µm. (D) Reduced number of striatal synapses in KO mice shown by VAMP2 staining, and (E) transmission electron microscopy. Behavioral analysis of 15 male WT and KO adult mice identified a striatal dysfunction with (F) reduced motivation analyzed by the progressive ratio schedule, increased catalepsy upon the i.p. injection of saline, and reduced sensory gating analyzed by pre-pulse inhibition of the startle reflex. Data are shown as Tukey plots, *<0.05 Mann Whitney test.

We conclude that NECAB2 orchestrates an endosomal pathway of mitochondrial quality control. Loss of this pathway results in synapse loss and striatal dysfunction.

Discussion

We here describe a novel endosomal mitochondrial stress response mediated by the Ca^{2+}-binding protein NECAB2. Mitochondria from *Necab2* knockout mice are more abundant but less efficient. They exhibit increased respiration and superoxide production but reduced mitochondrial ATP generation. Absence of this pathway causes loss of striatal synapses and behavioral phenotypes related to striatal dysfunction like reduced motivation, increased catalepsy and altered sensory gating.

Our data reveal a novel function of NECAB2 at intracellular membranes that is distinct from its function at the plasma membrane, where NECAB2 boosts basal constitutive signaling of striatal GPCR by direct interaction and increased surface localization. As the interaction with GPCRs is reversed by increased Ca^{2+} levels (Canela *et al*, 2009; 2007), it is probable that Ca^{2+} binding to the EF hands results in a conformational change of NECAB2 that triggers dimerization at intracellular membranes and activation of its novel function. In line with this observation, we found more dimerized NECAB2 in mitochondrial fractions.

Elevated cytosolic Ca^{2+} levels are the consequence of synaptic stimulation, which results in Ca^{2+} entry from the extracellular space through the activation of synaptic ionotropic NMDA channels and release from intracellular stores by the activity of extrasynaptic Gq-coupled receptors like the NECAB2-interacting metabotropic glutamate receptor mGluR5. Higher cytosolic Ca^{2+} levels can however also indicate neuronal dysfunction (Connolly & Prehn, 2015). Defective mitochondria are characterized by excessive production of reactive oxygen species and increased cytosolic Ca^{2+} levels; both alterations amplifying each other (reviewed by (Rizzuto *et al*, 2012)).

We now show that NECAB2 serves to keep synaptic mitochondria efficient by activating an endosomal mitochondrial quality control mechanism, likely through Ca^{2+}-dependent dimerization. NECAB2 assists repair or degradation of synaptic mitochondria by assembling RAB5 and the endosomal ESCRT machinery at mitochondria or the mitochondrial boundary. NECAB2 appears to be required for the recently-described mitochondrial stress response

where the RAB5 guanine exchange factor ALS2/Alsin mediates translocation of RAB5 from early endosomes to mitochondria upon oxidative stress (Hsu *et al*, 2018). Ca^{2+}-dependent repair mechanisms involving the ESCRT machinery have been described for the plasma membrane where assembly of ESCRT proteins at the site of repair is initiated by the Ca^{2+}-binding protein ALG-2 (apoptosis-linked gene 2) (Scheffer *et al*, 2014) leading to pinching out and shedding of wounded membranes (Jimenez *et al*, 2014). In contrast to autophagosomes, which are synthesized *de novo* on demand (Rubinsztein *et al*, 2012), early endosomes are continuously synthesized and exist as a network in all cells (Zeigerer *et al*, 2012) and dendritic spines (Cooney *et al*, 2002). This finding suggests that they can serve as a first line of defense when mitochondrial function is compromised or when highly efficient mitochondria are needed to provide energy for synaptic signaling.

NECAB2 is prominently expressed at striatal synapses where it associates with synaptic mitochondria. Synaptic mitochondria provide most of the energy needed to reverse the ion movements that generate postsynaptic responses. Interestingly, the number of mitochondria in synaptic terminals even exceeds the predicted energy needs, which implies additional functions (Harris *et al*, 2012), including the buffering of intra-spine Ca^{2+} levels that directly influence the firing probability of neurons (Devine & Kittler, 2018; Kwon *et al*, 2016). Depletion of local mitochondrial compartments also abolishes stimulus-induced synaptic translation and morphological plasticity of synapses (Rangaraju *et al*, 2014). Because active glutamatergic synapses on the spines of MSNs receive massive glutamatergic input from both the cortex and thalamus and dopaminergic input from the midbrain, they have even higher energy demands than other neurons. Striatal morphology in mice and primates treated with the mitochondrial complex II inhibitor 3-nitropropionic acid closely resembles the features observed here with fewer dendrites and more spines (reviewed by (Brouillet *et al*, 2005)). Intriguingly, knockout of MIRO1, another EF hand protein that anchors mitochondria at highly active synapses, diminishes the number of dendrites similar to NECAB2 deficiency (López-Doménech *et al*, 2016). Taken together, an activity-dependent increase in mitochondrial maintenance is specifically required at striatal synapses, where NECAB2 serves as an essential, new regulator of mitochondrial quality control.

The observations that the NECAB2 dimer prevails at the mitochondrial/endosomal interface, together with the facts that prokaryotic ABM domains are dimers (Lemieux *et al*, 2005; Sciara *et al*, 2003) and that the ABM domain of NECAB2 is necessary for dimerization suggest a role for the enzymatic ABM domain of NECAB2 in the process of mitochondrial quality control. Interestingly, ABM domain proteins are only present in plants and prokaryotes and again in the superphylum deuterostomia (which includes vertebrates but not insects or worms) meaning that they most probably entered this lineage through horizontal gene transfer. In prokaryotes, these enzymes are selectively expressed under low-iron conditions and convert

heme to ferrous iron (Fe^{2+}) and different metabolites such as staphylobilin (Skaar *et al,* 2004), formaldehyde (Matsui *et al,* 2013), and mycobilin (Nambu *et al,* 2013). Interestingly, endosome-mitochondrial contact in eukaryotes seems to involve the transfer of iron which is necessary for the production of iron-sulfur cluster proteins, one of the key functions of mitochondria in addition to oxidative phosphorylation and Ca^{2+} buffering (Hamdi *et al*, 2016; Das *et al*, 2016; Sheftel *et al*, 2007). However, this role has been so far exclusively described in blood cells. It remains to be investigated whether NECAB2 is involved in the transfer of iron from endosomes to mitochondria in neurons.

Mitochondrial dysfunction is involved in many neurodegenerative diseases (Johri & Beal, 2012). Here, circumstantial evidence suggests that NECAB2 dysfunction might play a role in two distinct diseases, amyotrophic lateral sclerosis (ALS) and Parkinson's disease (PD). On the one hand, the endosomal mitochondrial quality control mechanism triggered by oxidative stress (Hsu *et al*, 2018), which – at least in MSNs – relies on NECAB2, depends on the RAB5 guanine exchange factor ALS2/Alsin. Homozygous ALS2 mutation causes familiar ALS, a disease predominantly affecting peripheral and central motoneurons (Weishaupt *et al*, 2016). NECAB2 is strongly expressed in peripheral α-motoneurons in the ventral horn of the spinal cord (Zhang *et al*, 2014) making it possible that NECAB2-mediated mitochondrial quality control is involved in the pathomechanism associated with ALS2 mutation. On the other hand, NECAB2 is also strongly expressed in the substantia nigra (Fig. 1A) and degeneration of dopaminergic neurons in the substantia nigra causes PD. NECAB2 was found to be upregulated in dopaminergic neurons from patients with sporadic PD, monogenic PD associated with mutations in Leucine-rich repeat serine/threonine-protein kinase 2 (LRRK2) (Santiago *et al*, 2015) and in neurons from patients harboring mutations in the acid β-glucocerebrosidase (GCase) gene (GBA1) (Schöndorf *et al*, 2014). Mutations in GBA1 constitute the strongest genetic risk factor for PD known to date (Shulman *et al*, 2011). GCase and LRRK2 both play a role in endomembrane trafficking (Roosen & Cookson, 2016) similar to NECAB2. These results suggest that increased NECAB2 can somehow compensate for the alterations instigated by pathophysiological alterations linked to different PD etiologies. Our data also support the idea that loss of NECAB2 function results in a compensatory upregulation of the recently described ESCRT-dependent pathway of mitochondrial quality control that involves the ubiquitin ligase Parkin (Hammerling *et al*, 2017) which further links NECAB2 function to Parkinson's disease.

In summary, our work has identified a novel pathway in mitochondrial quality control in the striatum. The widespread expression of NECAB2 also suggests a role for this mechanism in other brain regions and in neurodegenerative diseases such as Parkinson's disease and amyotrophic lateral sclerosis.

Acknowledgment

This work was supported by the Deutsche Forschungsgemeinschaft (ME1922/14-1) to AM and the German Ministry of Education and Research (BMBF; GeNeRARe 01GM1519A) to MJS. The IMB Core Facility Microscopy and the Core facility for electron microscopy (CFEM, Heinrich Heine University Düsseldorf, Medical faculty) are gratefully acknowledged for their support. We are grateful to Hilmar Bading, Department of Neurobiology and Interdisciplinary Center for Neurosciences, Heidelberg University, in whose laboratory the electron microscopy work of the synaptosomes was carried out. The article contains results of the MD theses of Elena Morpurgo and Lena Sessinghaus. We thank Elizabeth Jane Rushing for excellent proofreading.

Author contributions

Performed experiments: PND, DB, TS, CW, VW, EM, LR, LS, PL, KR, MKES, LF, JB, PS, GH, LN, VV, AH, AO, RA. Analyzed data and wrote materials and methods: PND, DB, TS, CS, KR, LF, ST, JB, AD, AB, ASR, SR, MS, KBMF, AM. Wrote the manuscript: MS, AM

Declaration of Interests

No conflicts of interest.

Supplemental Figure 1: NECAB2 co-localizes with mitochondrial and endosomal but not autophagosomal or ER markers. NECAB2-mCherry co-localizes with endosomes (CD63-GFP) and mitoBFP2 but not with autophagosomes (LC3B-GFP) and the ER (ER-GFP) in transiently transfected HT22 cells. Size marker is 5 µm.

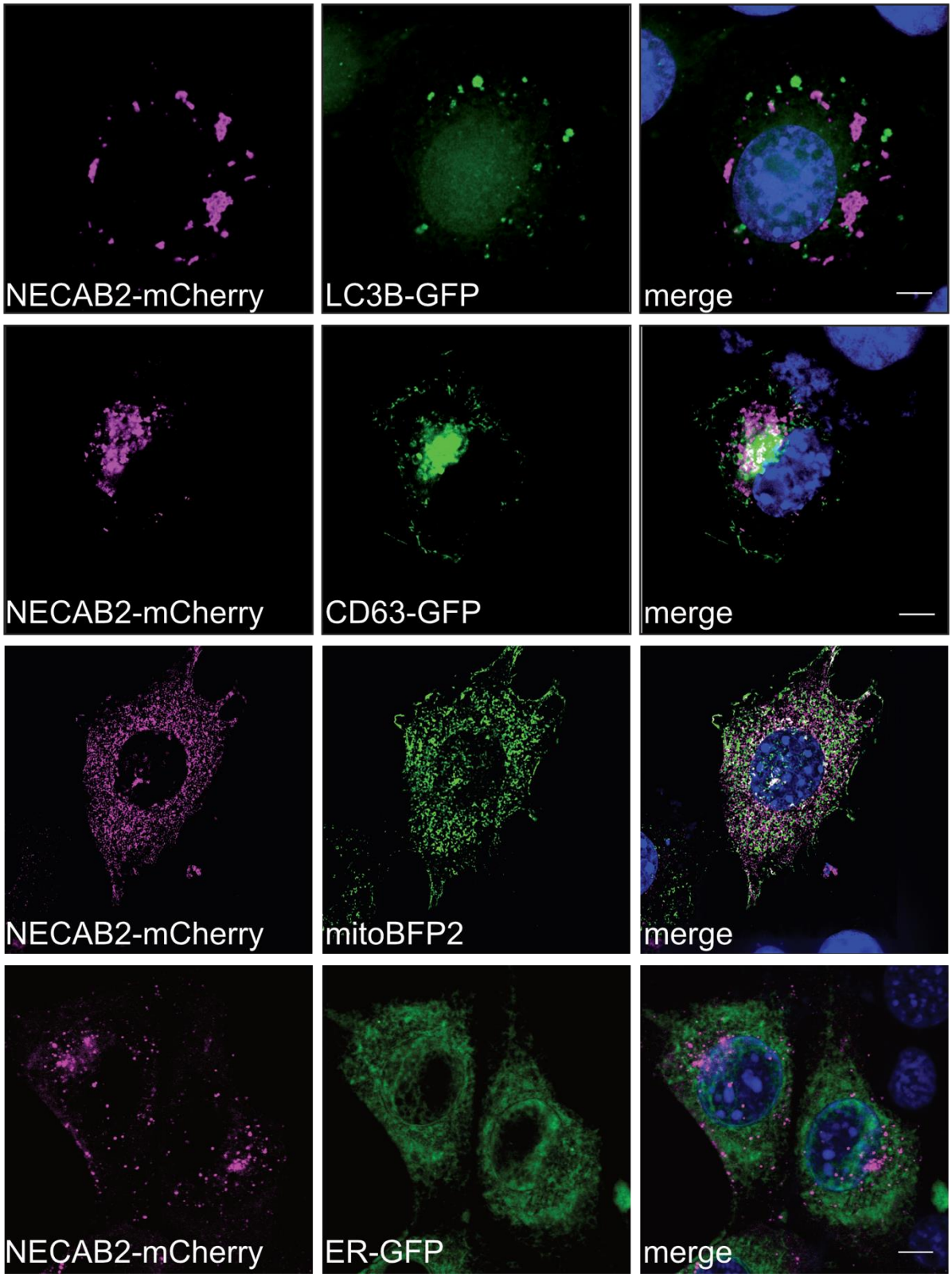

Supplemental Figure 2: Unimpaired basic locomotion and no differences in anxiety as tested by the open field test and the elevated plus maze test.

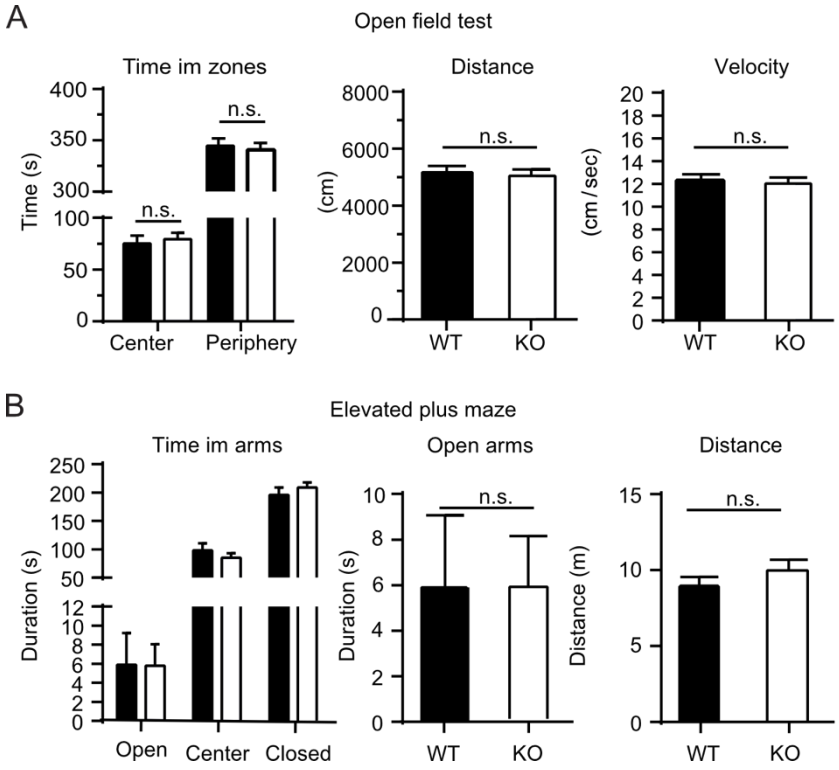

References

Anand R, Strecker V, Urbach J, Wittig I & Reichert AS (2016) Mic13 Is Essential for Formation of Crista Junctions in Mammalian Cells. *PLoS ONE* **11:** e0160258

Aniento F & Gruenberg J (2008) Subcellular Fractionation of Tissue Culture Cells Hoboken, NJ, USA: John Wiley & Sons, Inc. Available at: http://dx.doi.org/10.1002/0471140864.ps0403s32

Bates GP, Dorsey R, Gusella JF, Hayden MR, Kay C, Leavitt BR, Nance M, Ross CA, Scahill RI, Wetzel R, Wild EJ & Tabrizi SJ (2015) Huntington disease. *Nat Rev Dis Primers* **1:** 15005

Baumgart J & Grebe N (2015) C57BL/6-specific conditions for efficient in utero electroporation of the central nervous system. *J Neurosci Methods* **240:** 116–124

Bolte S & Cordelières FP (2006) A guided tour into subcellular colocalization analysis in light microscopy. *J Microsc* **224:** 213–232

Brouillet E, Jacquard C, Bizat N & Blum D (2005) 3-Nitropropionic acid: a mitochondrial toxin to uncover physiopathological mechanisms underlying striatal degeneration in Huntington's disease. *J. Neurochem.* **95:** 1521–1540

Canela L, Fernández-Dueñas V, Albergaria C, Watanabe M, Lluís C, Mallol J, Canela EI, Franco R, Luján R & Ciruela F (2009) The association of metabotropic glutamate receptor type 5 with the neuronal Ca2+-binding protein 2 modulates receptor function. *J. Neurochem.* **111:** 555–567

Canela L, Luján R, Lluís C, Burgueño J, Mallol J, Canela EI, Franco R & Ciruela F (2007) The neuronal Ca(2+) -binding protein 2 (NECAB2) interacts with the adenosine A(2A) receptor and modulates the cell surface expression and function of the receptor. *Mol. Cell. Neurosci.* **36:** 1–12

Clark IE, Dodson MW, Jiang C, Cao JH, Huh JR, Seol JH, Yoo SJ, Hay BA & Guo M (2006) Drosophila pink1 is required for mitochondrial function and interacts genetically with parkin. *Nature* **441:** 1162–1166

Connolly NMC & Prehn JHM (2015) The metabolic response to excitotoxicity - lessons from single-cell imaging. *J Bioenerg Biomembr* **47:** 75–88

Cooney JR, Hurlburt JL, Selig DK, Harris KM & Fiala JC (2002) Endosomal compartments serve multiple hippocampal dendritic spines from a widespread rather than a local store of recycling membrane. *J Neurosci* **22:** 2215–2224

Cox J & Witten IB (2019) Striatal circuits for reward learning and decision-making. *Nat Rev Neurosci* **20:** 482–494

Das A, Nag S, Mason AB & Barroso MM (2016) Endosome-mitochondria interactions are modulated by iron release from transferrin. *J. Cell Biol.* **214:** 831–845

Devine MJ & Kittler JT (2018) Mitochondria at the neuronal presynapse in health and disease. *Nat Rev Neurosci* **19:** 63–80

Distler U, Kuharev J, Navarro P & Tenzer S (2016) Label-free quantification in ion mobility-enhanced data-independent acquisition proteomics. *Nat Protoc* **11:** 795–812

Ferré S, Karcz-Kubicha M, Hope BT, Popoli P, Burgueño J, Gutiérrez MA, Casadó V, Fuxe K, Goldberg SR, Lluís C, Franco R & Ciruela F (2002) Synergistic interaction between adenosine A2A and glutamate mGlu5 receptors: implications for striatal neuronal function. *Proc Natl Acad Sci USA* **99:** 11940–11945

Frauenknecht K, Katzav A, Weiss Lavi R, Sabag A, Otten S, Chapman J & Sommer CJ (2014) Mice with experimental antiphospholipid syndrome display hippocampal dysfunction and a reduction of dendritic complexity in hippocampal CA1 neurons. *Neuropathol Appl Neurobiol***:** n/a–n/a

Gnaiger E, Kuznetsov A, Schneeberger S, Seiler R, Brandacher G, Steurer W & Margreiter R (2000) Mitochondria in the Cold. In *Life in the cold. Gerhard Heldmaier and Martin Klingenspor (Editors). 2000. Berlin, Heidelberg, New York: Springer-Verlag. x+ 546 p, illustrated, hard cover. ISBN 3- …*, Heldmaier G & Klingenspor M (eds) pp 431–442. Springer Berlin Heidelberg

Hackenbrock CR (1966) Ultrastructural bases for metabolically linked mechanical activity in mitochondria. I. Reversible ultrastructural changes with change in metabolic steady state in isolated liver mitochondria. *J. Cell Biol.* **30:** 269–297

Hamdi A, Roshan TM, Kahawita TM, Mason AB, Sheftel AD & Ponka P (2016) Erythroid cell mitochondria receive endosomal iron by a ‘kiss-and-run’ mechanism. *Biochim Biophys Acta* **1863:** 2859–2867

Hammerling BC, Najor RH, Cortez MQ, Shires SE, Leon LJ, Gonzalez ER, Boassa D, Phan S, Thor A, Jimenez RE, Li H, Kitsis RN, Dorn GW II, Sadoshima J, Ellisman MH & Gustafsson ÅB (2017) A Rab5 endosomal pathway mediates Parkin-dependent mitochondrial clearance. *Nature Communications* **8:** 14050

Harris JJ, Jolivet R & Attwell D (2012) Synaptic energy use and supply. *Neuron* **75:** 762–777

Higley MJ & Sabatini BL (2010) Competitive regulation of synaptic Ca2+ influx by D2 dopamine and A2A adenosine receptors. *Nat Neurosci* **13:** 958–966

Hollis F, van der Kooij MA, Zanoletti O, Lozano L, Cantó C & Sandi C (2015) Mitochondrial function in the brain links anxiety with social subordination. *Proc Natl Acad Sci USA* **112:** 15486–15491

Holmström MH, Iglesias-Gutierrez E, Zierath JR & Garcia-Roves PM (2012) Tissue-specific control of mitochondrial respiration in obesity-related insulin resistance and diabetes. *Am. J. Physiol. Endocrinol. Metab.* **302:** E731–9

Hsu F, Spannl S, Ferguson C, Hyman AA, Parton RG & Zerial M (2018) Rab5 and Alsin regulate stress-activated cytoprotective signaling on mitochondria. *Elife* **7:**

Jamain S, Radyushkin K, Hammerschmidt K, Granon S, Boretius S, Varoqueaux F, Ramanantsoa N, Gallego J, Ronnenberg A, Winter D, Frahm J, Fischer J, Bourgeron T, Ehrenreich H & Brose N (2008) Reduced social interaction and ultrasonic communication in a mouse model of monogenic heritable autism. *Proc Natl Acad Sci USA* **105:** 1710–1715

Jimenez AJ, Maiuri P, Lafaurie-Janvore J, Divoux S, Piel M & Perez F (2014) ESCRT machinery is required for plasma membrane repair. *Science* **343:** 1247136–1247136

Johri A & Beal MF (2012) Mitochondrial dysfunction in neurodegenerative diseases. *J. Pharmacol. Exp. Ther.* **342:** 619–630

Kheramin S, Body S, Herrera FM, Bradshaw CM, Szabadi E, Deakin JFW & Anderson IM (2005) The effect of orbital prefrontal cortex lesions on performance on a progressive ratio schedule: implications for models of inter-temporal choice. *Behavioural Brain Research* **156:** 145–152

Koch M (1999) The neurobiology of startle. *Prog Neurobiol* **59:** 107–128

Kröller-Schön S, Steven S, Kossmann S, Scholz A, Daub S, Oelze M, Xia N, Hausding M, Mikhed Y, Zinßius E, Mader M, Stamm P, Treiber N, Scharffetter-Kochanek K, Li H, Schulz E, Wenzel P, Münzel T & Daiber A (2014) Molecular mechanisms of the crosstalk between mitochondria and NADPH oxidase through reactive oxygen species-studies in white blood cells and in animal models. *Antioxid Redox Signal* **20:** 247–266

Kwon S-K, Hirabayashi Y & Polleux F (2016) Organelle-Specific Sensors for Monitoring Ca(2+) Dynamics in Neurons. *Front Synaptic Neurosci* **8:** 29

Lemieux MJ, Ference C, Cherney MM, Wang M, Garen C & James MNG (2005) The crystal structure of Rv0793, a hypothetical monooxygenase from M. tuberculosis. *J. Struct. Funct. Genomics* **6:** 245–257

Lewerenz J, Klein M & Methner A (2006) Cooperative action of glutamate transporters and cystine/glutamate antiporter system Xc- protects from oxidative glutamate toxicity. *J. Neurochem.* **98:** 916–925

Lojek LJ, Farrand AJ, Wisecaver JH, Blaby-Haas CE, Michel BW, Merchant SS, Rokas A & Skaar EP (2017) Chlamydomonas reinhardtii LFO1 Is an IsdG Family Heme Oxygenase. *mSphere* **2:**

López-Doménech G, Higgs NF, Vaccaro V, Roš H, Arancibia-Carcamo IL, MacAskill AF & Kittler JT (2016) Loss of Dendritic Complexity Precedes Neurodegeneration in a Mouse Model with Disrupted Mitochondrial Distribution in Mature Dendrites. *CellReports* **17:** 317–327

Lyles KV & Eichenbaum Z (2018) From Host Heme To Iron: The Expanding Spectrum of Heme Degrading Enzymes Used by Pathogenic Bacteria. *Front Cell Infect Microbiol* **8:** 198

Matsui T, Nambu S, Ono Y, Goulding CW, Tsumoto K & Ikeda-Saito M (2013) Heme degradation by Staphylococcus aureus IsdG and IsdI liberates formaldehyde rather than carbon monoxide. *Biochemistry* **52:** 3025–3027

McWilliams TG, Prescott AR, Montava-Garriga L, Ball G, Singh F, Barini E, Muqit MMK, Brooks SP & Ganley IG (2018) Basal Mitophagy Occurs Independently of PINK1 in Mouse Tissues of High Metabolic Demand. *Cell Metab* **27:** 439–449.e5

Meschler JP, Conley TJ & Howlett AC (2000) Cannabinoid and dopamine interaction in rodent brain: effects on locomotor activity. *Pharmacol. Biochem. Behav.* **67:** 567–573

Nambu S, Matsui T, Goulding CW, Takahashi S & Ikeda-Saito M (2013) A new way to degrade heme: the Mycobacterium tuberculosis enzyme MhuD catalyzes heme degradation without generating CO. *Journal of Biological Chemistry* **288:** 10101–10109

Narendra D, Walker JE & Youle R (2012) Mitochondrial quality control mediated by PINK1 and Parkin: links to parkinsonism. *Cold Spring Harb Perspect Biol* **4:**

Novotny EJ, Singh G, Wallace DC, Dorfman LJ, Louis A, Sogg RL & Steinman L (1986) Leber's disease and dystonia: a mitochondrial disease. *Neurology* **36:** 1053–1060

Park J, Lee SB, Lee S, Kim Y, Song S, Kim S, Bae E, Kim J, Shong M, Kim J-M & Chung J (2006) Mitochondrial dysfunction in Drosophila PINK1 mutants is complemented by parkin. *Nature* **441:** 1157–1161

Pickrell AM, Fukui H, Wang X, Pinto M & Moraes CT (2011) The striatum is highly susceptible to mitochondrial oxidative phosphorylation dysfunctions. *J Neurosci* **31:** 9895–9904

Pisani A, Gubellini P, Bonsi P, Conquet F, Picconi B, Centonze D, Bernardi G & Calabresi P (2001) Metabotropic glutamate receptor 5 mediates the potentiation of N-methyl-D-aspartate responses in medium spiny striatal neurons. *Neuroscience* **106:** 579–587 Available at: http://www.sciencedirect.com/science/article/pii/S0306452201002974

Radyushkin K, Hammerschmidt K, Boretius S, Varoqueaux F, El-Kordi A, Ronnenberg A, Winter D, Frahm J, Fischer J, Brose N & Ehrenreich H (2009) Neuroligin-3-deficient mice: model of a monogenic heritable form of autism with an olfactory deficit. *Genes Brain Behav.* **8:** 416–425 Available at: http://dx.doi.org/10.1111/j.1601-183x.2009.00487.x

Rangaraju V, Calloway N & Ryan TA (2014) Activity-driven local ATP synthesis is required for synaptic function. *Cell* **156:** 825–835

Rizzuto R, De Stefani D, Raffaello A & Mammucari C (2012) Mitochondria as sensors and regulators of calcium signalling. *Nat Rev Mol Cell Biol* **13:** 566–578

Roosen DA & Cookson MR (2016) LRRK2 at the interface of autophagosomes, endosomes and lysosomes. *Mol Neurodegener* **11:** 73

Rubinsztein DC, Shpilka T & Elazar Z (2012) Mechanisms of autophagosome biogenesis. *Curr Biol* **22:** R29–34

Santiago RF, Carbajal IC, Castellano G, Torrent R, Richaud Y, Danés AS, Blasi RV, Pla AS, Mosquera JL, Soriano J, Barneo JL, Canals JM, Alberch J, Raya Á, Vila M, Consiglio A, Subero JIM, Ezquerra M & Tolosa E (2015) Aberrant epigenome in iPSC-derived dopaminergic neurons from Parkinson's disease patients. *EMBO Mol Med* **7:** 1529–1546

Sarraf SA, Raman M, Guarani-Pereira V, Sowa ME, Huttlin EL, Gygi SP & Harper JW (2013) Landscape of the PARKIN-dependent ubiquitylome in response to mitochondrial depolarization. *Nature* **496:** 372–376

Scheffer KD, Gawlitza A, Spoden GA, Zhang XA, Lambert C, Berditchevski F & Florin L (2013) Tetraspanin CD151 mediates papillomavirus type 16 endocytosis. *J Virol* **87:** 3435–3446

Scheffer LL, Sreetama SC, Sharma N, Medikayala S, Brown KJ, Defour A & Jaiswal JK (2014) Mechanism of Ca^{2+}-triggered ESCRT assembly and regulation of cell membrane repair. *Nature Communications* **5:** 5646

Schöndorf DC, Aureli M, McAllister FE, Hindley CJ, Mayer F, Schmid B, Sardi SP, Valsecchi M, Hoffmann S, Schwarz LK, Hedrich U, Berg D, Shihabuddin LS, Hu J, Pruszak J, Gygi SP, Sonnino S, Gasser T & Deleidi M (2014) iPSC-derived neurons from GBA1-associated Parkinson's disease patients show autophagic defects and impaired calcium homeostasis. *Nature Communications* **5:** 4028

Schuhmacher S, Oelze M, Bollmann F, Kleinert H, Otto C, Heeren T, Steven S, Hausding M, Knorr M, Pautz A, Reifenberg K, Schulz E, Gori T, Wenzel P, Münzel T & Daiber A

(2011) Vascular dysfunction in experimental diabetes is improved by pentaerithrityl tetranitrate but not isosorbide-5-mononitrate therapy. *Diabetes* **60:** 2608–2616

Sciara G, Kendrew SG, Miele AE, Marsh NG, Federici L, Malatesta F, Schimperna G, Savino C & Vallone B (2003) The structure of ActVA-Orf6, a novel type of monooxygenase involved in actinorhodin biosynthesis. *EMBO J.* **22:** 205–215

Sheftel AD, Zhang A-S, Brown C, Shirihai OS & Ponka P (2007) Direct interorganellar transfer of iron from endosome to mitochondrion. *Blood* **110:** 125–132

Shulman JM, De Jager PL & Feany MB (2011) Parkinson's disease: genetics and pathogenesis. *Annu Rev Pathol* **6:** 193–222

Sielaff M, Kuharev J, Bohn T, Hahlbrock J, Bopp T, Tenzer S & Distler U (2017) Evaluation of FASP, SP3, and iST Protocols for Proteomic Sample Preparation in the Low Microgram Range. *J. Proteome Res.* **16:** 4060–4072

Skaar EP, Gaspar AH & Schneewind O (2004) IsdG and IsdI, heme-degrading enzymes in the cytoplasm of Staphylococcus aureus. *J. Biol. Chem.* **279:** 436–443

Thibault D, Loustalot F, Fortin GM, Bourque M-J & Trudeau L-E (2013) Evaluation of D1 and D2 dopamine receptor segregation in the developing striatum using BAC transgenic mice. *PLoS ONE* **8:** e67219

Weishaupt JH, Hyman T & Dikic I (2016) Common Molecular Pathways in Amyotrophic Lateral Sclerosis and Frontotemporal Dementia. *Trends in molecular medicine* **22:** 769–783

Wieckowski MR, Giorgi C, Lebiedzinska M, Duszynski J & Pinton P (2009) Isolation of mitochondria-associated membranes and mitochondria from animal tissues and cells. *Nat Protoc* **4:** 1582–1590

Yoshida T, Kakizuka A & Imamura H (2016) BTeam, a Novel BRET-based Biosensor for the Accurate Quantification of ATP Concentration within Living Cells. *Sci. Rep.* **6:** 39618

Zeigerer A, Gilleron J, Bogorad RL, Marsico G, Nonaka H, Seifert S, Epstein-Barash H, Kuchimanchi S, Peng CG, Ruda VM, Del Conte-Zerial P, Hengstler JG, Kalaidzidis Y, Koteliansky V & Zerial M (2012) Rab5 is necessary for the biogenesis of the endolysosomal system in vivo. *Nature* **485:** 465–470

Zhang M-D, Tortoriello G, Hsueh B, Tomer R, Ye L, Mitsios N, Borgius L, Grant G, Kiehn O, Watanabe M, Uhlén M, Mulder J, Deisseroth K, Harkany T & Hökfelt TGM (2014) Neuronal calcium-binding proteins 1/2 localize to dorsal root ganglia and excitatory spinal neurons and are regulated by nerve injury. *Proc Natl Acad Sci USA*

MATERIALS AND METHODS

Mice

Animal studies were performed according to the guidelines of the German Animal Welfare Act and Directive 2010/63/EU for the protection of animals used for scientific purposes and was approved by the Rhineland-Palatinate State Authority. Reporting was done in accordance to the Animal Research: Reporting of *In Vivo* Experiments (ARRIVE) guidelines. 3-12 weeks old mice (Necab2tm1a(KOMP)Wtsi (Necab) line) were housed in type II long, filter-top cages (Tecniplast, Buguggiate, Italy; SealSafe Plus, polyphenylsulfone, 365mm L x 207mm W x 140mm H Greenline) with enrichment. The mice were maintained under a 12:12-h light/dark cycle (lights on 06:00–18:00) in a temperature- and humidity-controlled animal room (22±2°C, 55±5%). Food (ssniff M-Z Extrudat, ssniff, Soest, Germany) and water were supplied ad libitum.

Primary neuronal culture

Primary striatal neurons were cultured from embryonic day 17 (E17). Embryos were obtained from pregnant NECAB2 heterozygous females. *Necab2* KO and WT brains were removed from the skull and placed in cold Hank's buffer without Ca^{2+} and Mg^{2+} (HBSS -/-). The cerebellum and brainstem were separated. Under a dissecting microscope striatal tissue was dissected and pooled separately after removal of the meninges. Dissected tissues of each embryo were kept separately, and the tails were collected for post genotyping. Tissues were washed once with HBSS -/- buffer, replaced with fresh 5 ml of HBSS -/- and digested for 15 min at 37ºC with trypsin/EDTA (10X, Sigma Aldrich, St. Louis, USA). DNaseI (Sigma Aldrich, St. Louis, USA) (50 g/ml) was also added at the same time of trypsinization. Tissues were then washed twice with plating media containing serum [Neurobasal medium (Thermo Fisher Scientific, Waltham, USA) supplemented with 2% B27 (Thermo Fisher Scientific, Waltham, USA), 1% Glutamax (Thermo Fisher Scientific, Waltham, USA), 1 µg/ml penicillin/streptomycin (Sigma Aldrich, St. Louis, USA) and 5% FCS (Thermo Fisher Scientific, Waltham, USA)] to quench the trypsin and dissociated into a single-cell suspension by gentle repeated passages through a sterile glass pipette.

For biochemical experiments, striatal neurons were plated at a density of 50K per well onto 24 well plates or 20K per well onto 8 well chamber slides coated with poly-L-lysine (Sigma Aldrich, St. Louis, USA) (100 µg/ml). Cells were maintained in plating media with serum for 3-4 hours and later replaced with Neurobasal media without serum [supplemented with 2% B27, 1% Glutamax and 1 µg/ml penicillin /streptomycin]. Neurons were incubated at 37°C with 5% CO_2. The sex of the cells was not determined. A solution of 10 mM 5-fluoro-2'-deoxyuridine and uridine (anti-mitotic agent) (Sigma Aldrich, St. Louis, USA) was added to the cultures at days in vitro (DIV) 3-6 to prevent glial overgrowth.

Human tissue

We used small amounts of anonymized archival surplus post-mortem brain tissue from the Institute of Neuropathology, University Hospital Zurich, Switzerland. The research project did not fall within the scope of the Human Research Act (HRA), thus an authorization of the ethics committee was not required (Cantonal Ethics Committee of Zurich; BASEC-No. Req-2020-00420). [R1]

Cell lines

The hippocampal HT22 cell line was used in the present study. The cells were grown in DMEM high glucose (Sigma-Aldrich, St. Louis, USA) supplemented with 5% Fetal Bovine Serum (FBS; Hyclone, Logan, USA) and 1% Penicillin/Streptomycin (Sigma-Aldrich, St. Louis, USA) at 37°C and 5% CO_2. The mEF and deletion mutants were obtained by gene synthesis, verified by sequencing, and cloned into the Piggybac vector pBac-CAG-HA-Dest-IRES-BFP2 using the Gateway system from Invitrogen (Waltham, USA). 48 hours after transfection of the constructs together with the hy-pBase Piggybac enzyme, stable HT22 cell lines were obtained by repeated cell sorting using a BD FACSAria™ III system (BD Biosciences, Franklin Lakes, USA) until more than 80% of cells were BFP2 positive.

Tissue preparation and immunohistochemistry

Brains were perfused with 4% formaldehyde in phosphate buffer saline (PBS), washed with phosphate buffer (PB) and embedded with paraffin. Coronal sections of 3 µm thickness were cut at the level of the hippocampus using a microtome (Leica Microsystems, Wetzlar, Germany). For immunohistochemistry either paraffin sections that were washed with 0.5% sodium azide (2 x 5 min) or directly cut coronal vibratome sections of 50 µm thickness were used. For the free-floating method the sections were washed several times with PB and blocked with 5% normal goat serum, 0.5% Triton X-100 in the PB for one hour. Primary antibodies, anti-NECAB2, 1:1000 (Sigma Aldrich, St. Louis, USA); Alexa-488 tagged cytochrome *c* antibody (BD Biosciences, Franklin Lakes, USA); anti-synaptobrevin 2 (VAMP), 1:1000, (Synaptic Systems, Göttingen, Germany); as well as the secondary antibodies goat anti-mouse Alexa 488 (1:1000), goat anti-mouse Alexa 568 (1:1000), goat anti-rabbit Alexa 488 (1:1000), goat-anti-rabbit Alexa 568 (1:1000) (all Millipore, Burlington, USA) were applied sequentially for 3 hours each. After several washing steps with PB, the sections were stained with 100 nM DAPI for 15 minutes and then mounted on glass slides with ProLong Gold (Invitrogen, Carlsbad, USA). Fluorescence pictures were taken with the same settings from one optical section using a 63x/1.4 oil immersion objective with the confocal microscope TCS SP5 (Leica Microsystems, Wetzlar, Germany). For co-staining of NECAB2 and cytochrome *c*, images were acquired using an Ultraview spinning disk confocal microscope (Perkin Elmer, Waltham, USA).

For the NECAB2/VGLUT1/VGLUT2 staining, mice were transcardially perfused with phosphate buffer saline (PBS) (5 minutes at 52 rpm) and 4% formaldehyde (PFA) in PBS (5 minutes at 52 rpm). Brains were then removed and stored at 4°C in PBS with 0.01% sodium azide until cutting. Sections of striatum (bregma coordinates from +1.69 mm to -0.83 mm according to Paxinos and Franklin, 5th edition, 2019), 40 µm thick, were cut with a vibratome (Leica VT1000S). Mouse brain sections were washed in PBS and blocked in 10% normal goat serum (NGS) and 0,1% Triton X-100 in PBS for one hour. The primary antibodies, anti-NECAB2, 1:250, (Sigma Aldrich, St. Louis, USA); anti-VGLUT1, 1:250, Synaptic Systems; Anti-VGLUT2, 1:250, Synaptic Systems were applied in 5% NGS and 0.1% Triton overnight at 4°C. After several washing steps, secondary antibodies (goat-anti-rabbit Alexa 488, (1:1000) and goat-anti-guinea pig Alexa 568, (1:1000) were applied in 5% NGS and 0.1% Triton for one hour at room temperature. DAPI (1:1000) was applied in PBS for an additional 15 minutes. Sections were washed in PBS, then mounted on a glass slide with Fluoromount G (Thermo Fisher Scientific). Pictures were taken with the confocal multiphoton microscope TCS SP8 (Leica Microsystems, Germany) using 40x and 63x oil immersion objectives.

For the sections of paraffin-embedded mouse brain: Endogenous peroxidase was blocked using 1 ml H_2O_2 (30%) in 100 ml methanol/PBS and then incubated for 30 min with 250 µl 5 % normal goat serum (NGS) in PBST. Sections were then incubated with the respective primary antibodies overnight at 4°C with polyclonal anti-NECAB2 or polyclonal anti-8-Hydroxydeoxyguanosine. After washing, sections were incubated with Vectastain Kit universal for 30 min, respectively. Afterwards sections were washed, and immunoreactivity was visualized by the avidin-biotin complex method and sections were developed in diaminobenzidine (DAB, Sigma Aldrich, St. Louis, USA).

Human brain sections were dewaxed through graded alcohols and pretreated in LEICA Buffer HIER2 (60 min, 100°C). Sections were automatically stained with Bond autostainer (Leica Microsystems, Wetzlar, Germany) using primary antibody against NECAB2, 1:200 (Sigma Aldrich); for 30 min. Finally, sections were developed using a Bond Polymer Refine Red Detection Kit (Leica Microsystems, Wetzlar, Germany).

Immunocytochemistry

Striatal neurons were plated on coverslips coated either with a mixture of 0.5 mg/ml PDL solution (Sigma Aldrich, St. Louis, USA), 1 mg/ml collagen solution (Thermo Fisher Scientific, Waltham, USA) and 17 mM acetic acid solution or with PLL solution (0.1 mg/ml). HT22 cells were seeded onto coverslips and transfected with mcherry-NECAB2 plus CD63-GFP, LC3B-GFP, Mito-BFP or ER-GFP.

DIV 12 MSNs or the transfected cells were fixed with 4% Roti®-Histofix (20 min at RT) and permeabilized with 0.25% Triton X-100 (Thermo Fisher Scientific, Waltham, USA) in PBS for

10 minutes at RT. The coverslips were blocked with Roti®-ImmunoBlock 1X (Carl Roth, Karlsruhe, Germany) for 30 minutes to 1 hr, followed by incubation with primary antibodies anti-NECAB2, 1:500 (Sigma Aldrich, St. Louis, USA), anti-Rab5, 1:200 (Santa Cruz, Dallas, USA), anti-Tom20, 1:400 (Sigma Aldrich, St. Louis, USA) at 4°C with gentle shaking overnight. The neurons or the transfected cells were washed and reprobed with fluorescent conjugated secondary antibodies in 1X Roti®-ImmunoBlock in dark condition at room temperature for 1 hr. Coverslips were stained with 300 nM DAPI for 5 min at RT and mounted onto microscope slides with Dako Fluorescence Mounting Medium. Fluorescence pictures were taken either with a confocal microscope (TCS SP5 or TCS SP8 – Leica Microsystems, Wetzlar, Germany) or with a Zeiss Axiovert 200 M (Carl Zeiss, Oberkochen, Germany) with deconvolution software using a 100x/1.4 oil immersion objective. Colocalization studies were performed using the JACoP plugin from ImageJ (Bolte & Cordelières, 2006) and/or using Imaris (BitPlane, Belfast, UK), where 3D images were generated from z-stacks. The colocalization degree of both channels were determined followed by quantification of dots of colocalizing signal, after applying a Background Subtraction (1.0) and Gaussian (0.1) filters. Alternatively, surfaces were generated from the fluorescent signal (threshold diameter size for mitochondria: 0.3 µm; endosomes: 0.4 µm; NECAB2 vesicles: 0.6 µm) on Imaris and the shortest distance between surfaces and the number of surfaces in contact were quantified.

Immunoblotting

Denatured total cellular protein samples (95°C, 5 min) from cells or brain tissue were separated on SDS polyacrylamide gels (4–15% Mini-PROTEAN® TGX Stain-Free™ gels, Bio-Rad, Hercules, USA) and transferred onto a membrane (nitrocellulose or PVDF) using the iBlot Dry Blotting System (Invitrogen, Carlsbad, USA) or Trans-Blot® Turbo™ Transfer System (Bio-Rad, Hercules, USA). Membranes were blocked with 3 or 5% (w/v) milk powder in PBS, PBS-T (1x PBS, 0.05% (v/v) Tween 20) or TBS-T (1x TBS, 0.05% (v/v) Tween 20) for 1 h at room temperature (RT). The membranes were incubated with the primary antibodies anti-NECAB2 1:1000 (Sigma Aldrich, St. Louis, USA), anti-VDAC 1:1000 (Cell Signaling, Danvers, USA), anti-COXIV 1:1000 (Cell Signaling, Danvers, USA), anti-b-tubulin 3, 1:2000 (R&D Systems, Minneapolis, USA), anti-HA, 1:3000 (Abcam, Cambridge, UK), anti-Myc, 1:3000 (Millipore, Burlington, USA), anti-PSD95, 1:1000 (Synaptic Systems, Göttingen, Germany), anti-b-actin mAB, 1:4000 (Millipore, Burlington, USA), anti-RAB5, 1:1000 (Santa Cruz, Dallas, USA) respectively, overnight at 4°C. For visualization, membranes were incubated with infrared fluorescence IRDye 680 and 800-conjugated anti-mouse/anti-rabbit IgG secondary antibodies, 1:30000 (LI-COR Biosciences, Lincoln, USA) for 1 h at RT and detected with the Odyssey Infrared or Odyssey Sa Infrared Imaging System (LI-COR Biosciences, Lincoln, USA). The software ImageJ or Image Studio™ Lite

Software (https://www.licor.com/bio/image-studio-lite/) was used to analyze the expression of proteins in relation to the control.

Autoradiography

Animals were decapitated and their brains were rapidly removed, blotted free of excess blood, immediately frozen in 2-methylbutane (-50°C) and stored until sectioning. Coronal sections (20 µm thickness) were produced in a microtome (Leica Microsystems, Wetzlar, Germany), thaw-mounted onto silane-coated slides and stored at -80°C until further use. All binding assays were preceded with a preincubation in the respective buffers for 15-30 min to remove endogenous transmitters. Adenosine A2A, dopamine D1 and D2 and metabotropic glutamate mGluR5 receptors as well as dopamine transporters (DAT) were labeled accordingly with [^{3}H]ZM241385 (0.42 nM), [^{3}H]SCH23390 (1.61 nM), [^{3}H]raclopride (0.59 nM), [^{3}H]ABP688 (2.23 nM) and [^{3}H]mazindol (4.07 nM) in 50 mM Tris-HCl (pH 7.4; 90 min at 22°C) containing in the pre- and main incubation EDTA (1 mM) buffer. Additionally, the main incubation adenosine deaminase (2 U/mL) in 50 mM Tris-HCl (pH 7.4; 90 min at 22°C) contains NaCl (120 mM), KCl (5 mM), $CaCl_2$ (2 mM) and $MgCl_2$ (1 mM). Furthermore, the main incubation mianserin (1 µM) in 50 mM Tris-HCl (pH 7.4; 45 min at 22°C) contain NaCl (150 mM) and ascorbic acid (0.1%) in 30 mM HEPES (pH 7.4; 65 min at 22°C) contain NaCl (40 mM), KCl (5 mM), $CaCl_2$ (2.5 mM) and $MgCl_2$ (1.2 mM) respectively or in the preincubation buffer 50 mM Tris-HCL (pH 7.9, 60 min at 4°C) contain 120 mM NaCl and 5 mM KCL and in the main incubation buffer 300 mM NaCl, 5 mM KCL with 300 nM desipramine using the displacers theophylline (5 mM), SKF 83566 (1 µM), butaclamol (1 µM), MPEP (10 µM) and nomifensine (100 µM), respectively. Brain tissue slices were washed two to six times in ice-cold buffer and rapidly rinsed in ice-cold distilled water, placed under a stream of cold air and exposed to phosphor-imaging plates (BAS-TR2025, Raytest, Straubenhardt, Germany) for three days together with tritium standards. Autoradiograms were scanned with a high-performance plate reader (BAS-5000, Raytest, Straubenhardt, Germany) and subsequently processed in a blinded manner using image-analysis software (AIDA 4.13, Raytest, Straubenhardt, Germany).

Subcellular fractionations

Endosomal fractions: Brains were removed from the *Necab2* KO and WT mice. The striatum was isolated and washed once with 5 ml PBS. After removing the supernatant, endosomal fractions were prepared as described in (Aniento & Gruenberg, 2008; Scheffer *et al*, 2013). The cell pellet was gently resuspended in 1.8 ml of homogenization buffer (HB: 250 mM sucrose, 3 mM imidazole, pH 7.4, 10 mM Tris–HCl, pH 7.4) using a wide pore tip (2 mm diameter). Afterwards, the homogenate was transferred to a 2 ml reaction tube and centrifuged for 10 min at 1500 x g at 4°C. The supernatant was removed, and the pellet was

resuspended in 0.5 ml of HB using a blue tip (1 ml). Immediately, the homogenate was quickly drawn ten times through a 22-G needle attached to a 1 ml syringe. The homogenate was centrifuged for 10 min at 1500 x g at 4°C. The post-nuclear supernatant (PNS) was taken for the sucrose gradient and diluted with a 62% sucrose solution (2.351 M sucrose, 3 mM imidazole, pH 7.4, 1 mM EDTA) to obtain a final concentration of 40.6%. The PNS sample was loaded to the bottom of a SW60 centrifuge tube and was overlaid with a 35% sucrose solution (1.177 M sucrose, 3 mM imidazole, pH 7.4). The next layer was a 25% sucrose solution (0.806 M sucrose, 3 mM imidazole, pH 7.4) and the homogenization buffer was used to fill up the centrifuge tube. The sucrose concentration was adjusted by monitoring the refractive index of each solution (1,3723 for 25%; 1,3904 for 35%; 1,4463 for 62%; 1,4001 for 40,6%). After centrifuging in a SW60 rotor for 90 min at 14000 x g, the gradient was fractionated in 300 µl steps. Early endosomes were enriched at the 25%/35% interface and late endosomes were located at the 25%/HB interface. The fractions were analyzed by immunoblotting (see above) and isolated endosomes were used for subsequent proteomics analyses.

Synaptic and non-synaptic mitochondria: All the steps were carried out at 4°C with extreme caution. Mouse brains were quickly removed and homogenized in a 4 ml Mito I buffer (0.32 M sucrose, 10 mM Tris-HCl pH 7.4, 1 mM EDTA, protease and phosphatase inhibitors) using a loosely fitting glass potter. Homogenized brains were further disrupted for 10 min using a cell disrupting bomb (Parr Instrument Company, Frankfurt am Main, Germany) by applying pressure of 60 bar of nitrogen gas, followed by the protocol as previously described in (Wieckowski *et al*, 2009) for isolation of mitochondria from animal tissue. Concisely, the homogenate was centrifuged with increasing speed and mitochondria were finally purified using a Percoll gradient method. The nuclear, cytosolic, crude and pure mitochondrial fractions were used for further analyses. Synaptic and nonsynaptic mitochondria were prepared adapting previously published protocols. Striata from 5 mice were pooled and homogenized with a Dounce homogenizer in a 5x volume of ice-cold isolation buffer containing 215 mM mannitol, 75 mM sucrose, 20 mM HEPES and 1 mM EGTA, pH: 7.2. The resultant homogenate was layered on a discontinuous gradient of 15%, 23%, and 40% (vol/vol) Percoll and centrifuged at 34,000 x g for 10 min. After centrifugation, band 2 (the interface between 15% and 23% containing synaptosomes) and band 3 (the interface between 23% and 40% containing nonsynaptic mitochondria) were removed from the density gradient. The fractions were washed by centrifugation at 16,500 x g for 15 min. The pellets were collected and resuspended in isolation buffer and the synaptosomal fraction was disrupted for 10 min using a cell disrupting bomb (Parr Instrument Company, Frankfurt am Main, Germany) by applying pressure of 1000 psi for 10 min. A second Percoll density gradient was prepared and the samples were layered for ultracentrifugation as described

above. Band 3 was obtained and resuspended in isolation buffer and the pellets were washed three times in isolation buffer without EGTA. The final synaptic and nonsynaptic mitochondrial pellets were resuspended in isolation buffer and stored on ice.

Synaptosomes: After homogenizing the brain tissue with 10 ml/1 g 0.32 M sucrose, 5 mM HEPES (pH 7.4), and protease inhibitor, the homogenate was centrifuged for 10 min, 1000 x g at 4°C and the supernatant (S1) was collected. The remaining pellet (P1) was homogenized as in the first step and then it was again centrifuged and the supernatant (S1') was collected. The supernatants S1 and S1` were combined and centrifuged at high speed for 15 min, 12.000 x g at 4°C. The supernatant (S2) was removed. The pellet included the synaptosome crude extract (P2). After washing, the pellet was dissolved and centrifuged for 20 min, 12000 x g at 4°C. The supernatant (S2`) was removed. The pellet included synaptosome crude extract (P2). After resuspending the pellet in 1.5 ml/1 g 0.32 M Sucrose, 5 mM HEPES (pH 8.1), and protease inhibitor, the pellet was loaded on a sucrose step gradient (SW40Ti: 10 ml tubes, 3 ml per gradient). Afterwards the gradient was centrifuged for 2 h, 26.000 rpm at 4°C in a Beckman Coulter Ultracentrifuge and the visible synaptosome layer was collected from the layer between 1 and 1.2 M sucrose. The synaptosome fractions were used for Western blot and electron microscopic analyses.

Label-free quantitative proteomic analysis

Whole striatal homogenates or pelleted endosomes (three to five replicate preparations from each genotype) were solubilized in 10 mM Tris, 1% SDS and digested using an optimized SP3 protocol previously described in (Sielaff *et al*, 2017). Prior to use, carboxylate-modified paramagnetic beads were rinsed and reconstituted in water at a concentration of 20 µg solids/µL. Lysates were reduced and alkylated using DTT and IAA, respectively. Afterwards, 2 µL of the prepared bead mix was added to the lysate and acetonitrile (ACN) was added to a final concentration of 70% (v/v). After short vortexing of the sample-bead mix, the sample was incubated for 18 min at room temperature. Subsequently, beads were immobilized by incubation on a magnetic rack for 2 min. The supernatant was discarded, and the pellet was rinsed with 70% (v/v) EtOH in water and 100% ACN. Beads were resuspended in 5 µL of 50 mM NH_4HCO_3 supplemented with trypsin at an enzyme-to-protein ratio of 1:25 (w/w). After overnight digestion at 37°C, ACN was added to reach a final concentration of 95% (v/v). After mixing and incubation, supernatant was removed, and beads were rinsed with 100% ACN. Peptides bound to the beads were eluted using 2% (v/v) dimethyl sulfoxide (DMSO) in water. Supernatant containing purified peptides was transferred into a fresh tube. Prior to LC−MS analysis, the peptides were acidified using 1% formic acid (FA). Digested peptides were separated by nanoUPLC on a 75 µm x 250 mm HSS-T3 column (Waters Corporation, Milford, USA) and analyzed using ion-mobility enhanced data-independent acquisition on a Waters Synapt G2-S mass spectrometer in three technical replicates as described in (Distler

et al, 2016). Raw data processing, database search and label-free quantification was performed as described before (Distler *et al*, 2016).

Transmission electron microscopy and image quantification

Synaptosomes were fixed with 2% glutaraldehyde in 0.1 M sodium phosphate buffer, pH 7.4. After washing, the samples were post-fixed with 2% osmium tetroxide/1.5% potassium ferrocyanide for 1 h on ice, washed, contrasted en bloc with uranyl acetate, dehydrated with an ascending series of ethanol and embedded in glycid ether 100-based resin. Ultrathin sections were cut with a Reichert Ultracut S ultramicrotome (Leica Microsystems, Wetzlar, Germany). After contrasting, they were viewed with a ZEISS EM 10 CR electron microscope at an acceleration voltage of 60 kV. The length, width and electron density of the mitochondria were analyzed with Fiji/ImageJ.

TEM of brain striatum was performed as described previously (Anand *et al*, 2016). Mice were fixated by performing whole body cardiac perfusion using freshly prepared 3.7% formaldehyde and 0.5% glutaraldehyde buffered in PBS. Perfused brain tissue was washed twice with 0.1 M sodium cacodylate buffer (pH 7.2). Small striatal tissue pieces of about 2 mm^3 size were prepared. Striatal tissue pieces were stained for 1 h with 1% OsO_4 in 0.1 M sodium cacodylate buffer (pH 7.2). Samples were washed three times for 10 min with aqua bidest prior to staining with 1% uranyl acetate in aqua bidest at 4°C overnight. Stained pieces were washed three times for 5 min with aqua bidest before subjecting them to a series of ethanol dehydration incubations: 1 × 20 min in 30% ethanol, 1 × 20 min in 50% ethanol, 1 × 30 min in 70% ethanol, 1 × 30 min in 90% ethanol, 1 × 30 min in 96% ethanol, 1 × 30 min in 100% ethanol. This was followed by resin infiltration incubations: 1 × 20 min in 50% resin (AGR1280; Agar Scientific, Stansted, UK) in 100% ethanol, 3 × 20 min in 100% resin. Finally, specimens were embedded in 100% resin in gelatin capsules and incubated for polymerization at 65°C for 16 h. A transmission electron microscope (Hitachi, H600) was used for image recording of ultrathin sections. Recordings were made at 75 V equipped with Bioscan model 792 (Gatan) camera.

Electron microscopic images of striatal mitochondria were analyzed using ImageJ. Each single image had a size of 1 μm^2. Length and width of each mitochondrion was measured by defining the spatial scale and also by measuring "Distance in Pixels". Each mitochondrion was identified and counted manually as regions of interest (ROI) and the average signal intensity (mean grey value) within the ROI was measured. The mean grey value of each selected ROI referred to the levels of density of each mitochondrion. Synapses were counted manually (blind and unbiased) and divided by the total area to obtain the number of synapses per μm^2.

High resolution respirometry in tissue

Mice were sacrificed by cervical dislocation immediately before analysis. Brains were micro-dissected on ice and dissected striata were directly transferred into ice-cold mitochondrial respiration medium MiR05 (Gnaiger *et al*, 2000). The striatum was then homogenized in a pre-cooled 1.5 ml tube with a motorized pestle. Resulting homogenates containing 10 mg tissue w/w were suspended in 100 ml of MiR05 and later 20 ml (2 mg) tissue suspension was added to each chamber of the Oroboros Instrument (Oroboros Instruments, Innsbruck, Austria) containing 2 ml of MiR05 for OXPHOS-analysis (Holmström *et al*, 2012).

Oxygen concentration (μM) as well as oxygen flux per tissue mass (pmol O2. $s^{-1} \cdot mg^{-1}$) were recorded in real-time using DatLab software (Oroboros Instruments, Innsbruck, Austria). A multi substrate protocol was used to sequentially explore the various components of mitochondrial respiratory capacity. The striatum homogenate was suspended in MiR05, added to the Oxygraph-2k glass chambers and the O_2 flux was allowed to stabilize. A substrate, uncoupler, inhibitor titration (SUIT) protocol was applied to assess qualitative and quantitative mitochondrial changes in NECAB2 KO mice and WT controls. After stabilization, LEAK respiration was evaluated by adding the complex I (CI) substrates malate (2 mM), pyruvate (10 mM) and glutamate (20 mM). Maximum oxidative phosphorylation (OXPHOS) capacity with CI substrates was attained by the addition of ADP+$MgCl_2$ (5 mM) (CI OXPHOS). For evaluation of maximum OXPHOS capacity of the convergent input from CI and complex II (CII) at saturating ADP concentration, the CII substrate succinate (10 mM) was added (CI+CII OXPHOS). We then uncoupled respiration to examine the maximal capacity of the electron transport system (ETS or CI+II ETS) using the protonophore, carbonyl cyanide 4 (trifluoromethoxy) phenylhydrazone (FCCP; successive titrations of 0.2 μM until maximal respiration rates were reached). We then examined consumption in the uncoupled state solely due to the activity of complex II by inhibiting complex I with the addition of rotenone (0.1 μM; ETS CII or CII ETS). Finally, electron transport through complex III was inhibited by adding antimycin A (2 μM) to obtain the level of residual oxygen consumption (ROX) due to oxidation side reactions outside of mitochondrial respiration. The O_2 flux obtained in each step of the protocol was normalized by the wet weight of the tissue sample used for the analysis and the ROX was subtracted from the fluxes in each run to correct for non-mitochondrial respiration (Hollis *et al*, 2015).

Mitochondrial membrane potential

Primary striatal neurons were plated in 8 well chamber slides 12 days prior to staining and were loaded with 25 nM TMRM in Tyrode solution (150 mM NaCl, 4 mM KCl, 2 mM $MgCl_2$, 2 mM $CaCl_2$, 10 mM glucose, 10 mM Hepes, pH 7.4) at room temperature for 30 min. Assessment of the mitochondrial membrane potential maintenance through application of the

uncoupler carbonyl cyanide-p-trifluoromethoxy phenylhydrazone (FCCP) was performed by recordings obtained from a single focal plane. A reduction in TMRM fluorescence represents mitochondrial depolarization. Measurements were obtained with a TCS SP5 confocal microscope (Leica Microsystems, Wetzlar, Germany) using a 40x oil immersion objective while keeping 25 nM TMRM in the imaging solution. TMRM was excited using the 560 nm laser line and fluorescence was measured at 580 nm. Image processing was performed using LAS AF lite software identifying regions of interest (ROI; e.g. individual cells, or mitochondrial-enriched regions), and measuring the average signal intensity within the ROI. For each ROI, plotted the signal intensity over time (absolute signal intensity) and compared mitochondrial membrane potential (Δψm) between *Necab2* KO and WT striatal neurons.

Measurement of cytoplasmic and mitochondrial ATP

Relative ATP levels were determined with BTeam, a BRET-based ATP biosensor (Yoshida *et al*, 2016). Primary striatal neurons were seeded into white 96-well plates at a density of 2000 cells/well. DIV12 MSNs were transiently transfected using Viafect reagent (Promega, Madison, USA) with BTeam lacking a targeting sequence (for cyto-ATP determination) or containing a mitochondrial targeting sequence (for mito-ATP determination). After 24-48 hrs, neurons were washed with Neurobasal media without serum and incubated for 30 min in phenol red-free Neurobasal medium, and 30 µM NanoLuciferase (NLuc) inhibitor (1:1000) to prevent unintended detection of BTeam released from dead neurons. After addition of NLuc substrate reagent with a dilution of 3:1000 to the medium, the microplates containing the striatal neurons were incubated at 37°C for 20 min. In the presence of NLuc substrate (Promega, Madison, USA), the luminescence was measured at 520/60 nm (ex/em) (Yellow Fluorescent Protein (YFP) emission) and at 430/70 nm (ex/em) (NLuc emission) at 37°C using a Spark® Multimode Microplate Reader by Tecan. Data are expressed as YFP/NLuc emission ratio.

Superoxide quantification

Primary cultures: DIV12–14 MSN were loaded with 5 µM MitoSOX diluted in Neurobasal medium without FCS, for 10-30 minutes at 37°C protected from light. The neurons were washed with PBS, and the fluorescence measurements were carried out at excitation - 510/emission - 580 nm, on a live cell imaging platform of a SP5 confocal microscopy (Leica Microsystems, Wetzlar, Germany). The mean of MitoSOX signals was measured and quantified using ImageJ software.

Striatal tissue: The brains of WT and *Necab2* KO mice were removed and one part of the striatum was isolated. The striatum tissue was resuspended in 500 µl PBS. After centrifugation, the supernatant was discarded, and the tissue resuspended and incubated in 20 µM myxothiazol solution in PBS (100 µl) for 20 min at RT. After another centrifugation

step, the supernatant was again discarded, and the tissue washed with 500 µl PBS. The tissues were incubated with 50 µM dihydroethidium (200 µl) for 30 min at RT in the dark. After centrifugation, the supernatants were collected for control measurements while the tissue pellet was resuspended in 200 µl PBS and stored on ice. The samples were diluted 1:1 with 100% acetonitrile and then centrifuged for 20 min at 20050 x g. 200 µl of the supernatant were transferred to a high-performance liquid chromatography (HPLC). The method was described in (Schuhmacher *et al*, 2011). DHE signal was detected by its absorption at 355 nm. The DHE signal was normalized to the wet weight of the striatum tissue.

Enzymatic measurement of total cellular GSH content

Striata were isolated from 3 or 12-month-old *Necab2* KO and WT mice. Striata were homogenized in 200 µl of 2 mM EDTA in cold PBS each in separated 1.5 ml tubes. Total cellular GSH content was quantified enzymatically as previously described (Lewerenz *et al*, 2006). The tissue homogenate was carefully washed twice with phenol red-free Neurobasal medium and incubated with 20 µM MCB for 5 min at 37°C protected from light. MCB fluorescence was measured by a SpectraMax I3 microplate reader. Excitation wavelength was 393 nm and emission wavelength 485 nm.

Behavioral tests

Fifteen male WT and *Necab2* KO mice (littermates) at 3-4 months of age underwent a battery of behavioral tests. All tests were performed in sound-attenuated rooms, between 9 am and 5 pm. Mice were grouped with access to food and water and a 12 h - 12 h light-dark cycle (light phase onset at 7.00 h). All experiments were performed with permission of the local authorities in accordance with the German Animal Protection Law. All experiments and initial quantitative analyses were performed blinded, i.e. the experimenter had no knowledge of the genotype of the mice tested and analyzed.

Progressive ratio test: Progressive ratio reinforcement task to evaluate motivation: Progressive ratio (increasing number of responses are required to obtain consecutive deliveries of the reward) reinforcement task provides reliable and unambiguous measure of incentive motivation. We conducted this task in the touch-screen-based operant conditioning system (Med Associates, St. Albans, VT, USA). The operant chamber (dimensions: 18.1 cm × 17.6 cm × 18.6 cm), enclosed in a sound and light attenuating box, contained a pellet dispenser, which delivered a single 14 mg dustless precision pellet (Test Diet, St. Louis, USA) into a food tray (magazine). A touch sensitive TFT monitor (touchscreen; 18.4 cm × 13.6 cm) was located on the opposite side of the chamber. The touchscreen was covered with a metal partition containing a response hole (2 cm in diameter), allowing presentation of

simple visual stimuli (light). Touch-screen-based progressive ratio reinforcement task was controlled by K-Limbic software (Conclusive Marketing Ltd, Herts, UK).

Touch-screen experimental procedures: Initially, a food deprivation regimen was introduced, and the mice were gradually reduced to 85% of their free-feeding body weights. Animals were kept on food deprivation regimen throughout the duration of the experiment. Mice were tested on 7 consecutive days per week. Every mouse underwent the following sequence of test phases: (1) reward habituation and chamber acclimation, (2) autoshaping, (3) pre-conditioning 1–3 and (4) progressive ratio reinforcement task. Daily sessions were terminated after 30 min or as soon as the mouse had accomplished the learning criterion of the respective test phase.

Reward habituation and chamber acclimation: First, mice were habituated overnight with reward pellets in their home cages. Next day an experimental chamber acclimation began: Pellets were freely available in the magazine with an inter-trial interval of 15 s. A new trial was initiated after collection of the pellet leading to a disruption of an infrared light beam. This phase was conducted daily for 30 min until the mouse reached the criterion: No pellets left in the magazine after finishing the session. Then the mouse was moved to the next phase.

Fixed ratio 1 (FR1): The session started with a reward pellet in a magazine. After the mouse had collected the pellet, a light stimulus was presented in the stimulus hole on the touchscreen. Stimulus was presented until touch-response of the mouse. Then, the stimulus light went OFF and light in the magazine went ON, signalizing delivery of the reward pellet. A next trial was initiated after collection of the pellet (inter-trial interval 15 s). This phase was conducted daily for 30 min until the mouse reached the criterion: Complete at least 30 trials, and then the mouse was moved to the next phase.

Fixed ratio 2 (FR2): This phase was performed exactly as FR1, with one exception: The mouse has to make 2 touch-responses in order to be rewarded. After reaching the criterion, the mouse was moved to the next phase.

Fixed ratio 4 (FR4): This phase was performed exactly as FR1, with one exception: The mouse has to make 4 touch-responses in order to be rewarded. After reaching the criterion, the mouse was moved to the final phase.

Progressive ratio (PR) (Kheramin *et al*, 2005). This phase was performed similarly as FR1. Progressive ratio means that a mouse has to progressively increase the number of responses (touches of the screen) in order to earn a reward pellet. The PR schedule (i.e. the number of responses mice have to do in order to get next reward) was based on the following exponential progression: 1, 2, 4, 6, 9, 12, 15, 20, 25, 32, 40, 50, . . . , derived from the formula [(5×e0.2n)−5], rounded to the nearest integer, where “n” is the position in the

sequence of ratios. The duration of this phase was 90 min. A number of completed (i.e. rewarded) trials was recorded for each mouse.

Catalepsy test: The bar test was adapted from Meschler *et al.* (Meschler *et al*, 2000). A metal bar (4mm in diameter) was horizontally positioned 6 cm above the desk surface. The animal's front paws were placed on the bar and the hind paws were rested on the desk. Time was recorded until the mouse placed both front paws onto the desk.

Prepulse inhibition test of sensory-motor gating (Koch, 1999): The test was performed as described earlier (Radyushkin *et al*, 2009). Briefly, mice were placed in small metal cages (90 × 40 × 40 mm) to restrict major movements. The cages were equipped with a movable platform floor attached to a sensor that records vertical movements of the floor. Cages were placed in four sound-attenuating isolation cabinets (Med Associates, St. Albans, USA). Startle reflexes were evoked by acoustic stimuli delivered from a loudspeaker suspended above the cage and connected to an acoustic generator. The startle reaction to an acoustic stimulus, which evokes a movement of the platform and a transient force resulting from this movement of the platform, was recorded with a computer during a recording window of 380 milliseconds (beginning with the onset of pre-pulse) and stored for further evaluation. An experimental session consisted of a 2-min habituation to 65 dB background white noise (continuous throughout the session), followed by a baseline recording for 1 min. After baseline recording, 8 pulse-alone trials using startle stimuli of 120 dB intensity and 40 milliseconds duration were applied in order to decrease the influence of within-session habituation. These data were not included in the analysis of the prepulse inhibition. For tests of prepulse inhibition, the 120 dB/40 milliseconds startle pulse was applied either alone or preceded by a pre-pulse stimulus of 70, 75- or 80-dB intensity and 20 milliseconds duration. An interval of 100 milliseconds with background white noise was employed between each pre-pulse and pulse stimulus. 10 trials of each kind (in total 40 trials) were applied in a pseudorandom order with variable inter-trial intervals ranging from 8 to 22 seconds. Amplitudes of the startle response were averaged for each individual animal, separately for each type of trials (i.e. stimulus alone or stimulus preceded by a pre-pulse f 3 intensity). Prepulse inhibition was calculated as the percentage of the startle response using the following formula: PPI (%) = 100 – [(startle amplitude after pre-pulse and pulse / startle amplitude after pulse only) × 100].

Open field test as described (Jamain *et al*, 2008): Instinctive movement in the open field was tested in a gray Perspex arena (120 cm in diameter, 25 cm high; illumination 120 lux). Mice were placed in the center and allowed to explore the open field for 7 min. The behavior was recorded by a PC-linked overhead video camera. “Ethovision XT” (Noldus Information Technology, Wageningen, Netherlands), a video-tracking software, was used to calculate

velocity, distance traveled, and time spent in central, intermediate or peripheral zones of the open field.

Elevated plus maze as described (Jamain *et al*, 2008): Individual mice were placed in the central platform facing an open arm of the plus-maze (made of grey Perspex with a central 5 x 5 cm central platform, two open arms, 30 x 5 cm, 2 enclosed arms, 30 x 5 x 15 cm, illumination 120 lux). Behavior was recorded by an overhead video camera and a computer equipped with “Ethovision XT” (Noldus Information Technology, Wageningen, The Netherlands) software to calculate the time each animal spent in open or closed arms. The relevant amount of time spent in open arms was used to evaluate open arm aversion, which is associated with fear.

Golgi-Cox staining and analysis

For Golgi-Cox analysis the PBS-perfused brains of WT (n=7) and *Necab2* KO (n=5) mice were processed as described (Frauenknecht *et al*, 2014). Briefly, brains were incubated in 20 ml Golgi-Cox solution for 14 days in the dark, then the solution was replaced with 30% sucrose and the brains were incubated at 4°C for at least 2 days until sectioning. Coronal sections of 150 µm thickness were serially cut with a vibratome (VT1000S, Leica, Germany). Sections were then collected on 2% gelatinized slides, rinsed with distilled water, and placed into ammonium hydroxide in the dark for 30 min. After rinsing with distilled water, sections were immersed for 30 min in Kodak Fix for Film diluted 1:1 with distilled water and subsequently washed with distilled water followed by dehydration in ascending alcohol series (1 min: 50%; 1 min: 70%, 1 min: 95%, 5 min twice: 100%). This was followed by 10 min in a solution of 33% ethanol, 33% HemoDe (limonene), 33% chloroform and by 15 min twice in HemoDe. The slides were covered with cover slips using Permount. A LEICA DM6000B microscope and a computer-based system (Neurolucida; MicroBrightField Bioscience, Williston, USA) were used to generate three-dimensional neuron tracings. Visualization and analysis of neuron morphology were performed using NeuroExplorer (MicroBrightField Bioscience, Williston, USA). Neurons were reconstructed by one investigator blinded to group identity using a camera lucida and a 40x objective. Dendritic parameters as well as 3D Sholl analysis to assess dendritic complexity were calculated for each neuron and for each animal as described { {Frauenknecht:2014kq}. The results were analyzed for apical and basal dendrites separately and were presented as means ± SEM. The density of dendritic spines of a distinct branch order (MSN: 2nd, 3rd and 4th order dendrites) was measured for each animal using a 100x oil-immersion objective (Leica Microsystems, Wetzlar, Germany). Dendritic spines visible along both sides of segments were counted on dendrites of distinct orders with a minimum length of 10 µm and were expressed as mean number of spines per µm.

In utero electroporation and spine quantification

In utero electroporation experiments were carried out essentially as described (Baumgart & Grebe, 2015). Borosilicate glass capillaries (0.8–0.9 mm in diameter, World Precision Instruments Inc., Sarasota, FL, USA) were pulled using a P-97 Micropipette Puller (Sutter Instrument Company, Novato, CA, USA). The tips were grinded at 35◦ angles (Microgrinder EG-44, Narishige, London, GB). The colored DNA solution containing the GFP-encoding plasmid (pCAGGS (Addgene, Cambridge, UK)) was injected into the striatum. The appropriate voltage was applied via specialized platinum electrodes (Nepagene CUY 650P (Nepagene, Ichikawa, Japan), interval cycle length 50 ms, interval pause 950 ms). The voltage was supplied by two types of electroporators (Nepagene CUY 21 (Nepagene, Ichikawa, Japan) or BTX ECM 830 (Harvard Apparatus Inc., Holliston, MA, USA)) that delivered identical results. Injection was made into the striatum. After birth, the electroporated mice were decapitated and perfused with 4% PFA at the age of P21. Staining on free-floating vibratome slices (40 µm) was done with anti-GFP (Abcam, Cambridge, UK). Pictures were taken with a 63x oil immersion objective on the confocal microscope TCS SP5 from Leica (Leica Microsystems, Wetzlar, Germany). Analysis and 3D construction were done with ImageJ and Imaris.

QUANTIFICATION AND STATISTICAL ANALYSIS

The Shapiro-Wilk test was used to determine normality of distribution of the data. Data normally distributed were analyzed with the one- or two-way ANOVA followed by the Tukey's test or with the independent t test. Data not-normally distributed were analyzed with the Kruskal-Wallis test followed by the Dunn's test or with the Mann-Whitney test. A *P* value lower than or equal to 0.05 was considered statistically significant. Values are reported as mean ± SEM. Additional analyses were performed using the general statistics module of Analyse-it™ for Microsoft Excel (Analyse-it Software Ltd., Leeds, UK) or by using GraphPad Prism (GraphPad, San Diego, USA). Further statistical details can be found in the figures legends.